Ternary phase-field simplified multiphase lattice Boltzmann method and its application to compound droplet dynamics on solid surface in shear flow

Z. Chen [1,2] C. Shu [2,*] Y. Y. Liu,[2] and L. Q. Zhang[3]

[1]*Temasek Laboratories, National University of Singapore, 5A Engineering Drive 1, Singapore 117411, Singapore*

[2]*Department of Mechanical Engineering, National University of Singapore, 10 Kent Ridge Crescent, Singapore 119260, Singapore*

[3]*College of Aerospace Engineering, Chongqing University, Chongqing 400044, People's Republic of China*

(Received 14 April 2021; accepted 25 August 2021; published 9 September 2021)

A ternary phase-field simplified multiphase lattice Boltzmann method (TPF-SMLBM) is developed and employed in numerical investigation of a compound droplet placed on solid substrate in shear flow at moderate Reynolds numbers. The TPF-SMLBM utilizes the simplified multiphase lattice Boltzmann method as the flow solver and the ternary phase-field model as the interface tracking algorithm. Compared with conventional lattice Boltzmann method, this method preserves advantages in memory cost and boundary treatment. The numerical investigations recover three major modes of motion, namely the quasisteady sliding, tumbling-sliding, and tumbling-detachment. The quasisteady sliding dynamics are analyzed from the perspective of energy conversion, which explains the exponential shrinking rate of the wetting length in early evolution stage. By using the force-balance analyses, the onset of tumbling motion is firstly elaborated as the breakup of the balance in quasisteady sliding. A dimensionless parameter named as the tumbling number $\mathrm{Tu} = \mathrm{Ca}/\mathrm{Re}^{-0.5}$, where Ca and Re are, respectively, capillary and Reynolds numbers, is proposed to identify the mode transition towards tumbling. The physical rational of this parameter can be established from both the force analyses and the balance of timescales, and is further validated by abundant simulation results which show that its criticality is roughly on the order of $O(1)$ in the low-density–viscosity ratio scenarios. For the tumbling-sliding mode, the re-adhesion of tumbling droplet portion generates extra diffusive flow behavior and shrinks the wetted length of the sliding droplet portion. The dynamics of detachment is also investigated, showing that the critical capillary number of detachments can be scaled by $\mathrm{Ca}_{c,\mathrm{detach}} \sim \mathrm{Re}^{-0.3}$.

DOI: 10.1103/PhysRevFluids.6.094304

I. INTRODUCTION

Droplet dynamics is of important value in both physical explorations and engineering applications. Compound droplet in a shear flow is a typical example of droplet dynamics problems which can be traced back to the very early attempts made by Chambers and Kopac [1]. It has been attracting increasing attention in recent years due to its potential values in some emerging technologies such as advanced cell handling, drug delivery, additive manufacturing, and enhanced oil recovery [2–8].

From the physical perspective, the compound droplet in a shear flow is at least a ternary fluid system [9]. Different portions of the droplet as well as the ambient fluid are separated by thin layers of interfaces on which the surface tensions are imposed. Complexities of this problem stem from

*mpeshuc@nus.edu.sg

various factors such as distinct fluid properties of different phases, density and viscosity contrasts, interfacial deformations, interactions with the solid surfaces, etc. These complexities are essentially dynamic outcomes of the force balances. To quantify the force balances, dimensionless parameters are commonly used. For a compound droplet in shear flow, interesting dimensionless parameters could be the Reynolds number (Re), which defines the ratio of inertial force to viscous force, the Weber number (We), which quantifies the ratio of inertial force to surface tension force, and the capillary number (Ca) representing the ratio of viscous force to interfacial force.

Explorations on the compound droplet with translating behaviors have been conducted in experimental, analytical, and numerical manners [10–13]. Specifically, numerical investigations of this topic have been primarily on the configurations of one or more minor droplets confined within another in a different phase. Abundant results have been reported on the migration, deformation, breakup, and interaction of the compound droplets in flow currents [14–19]. Some other studies have been addressing the issue of the compound capsules in shear flows, in which the droplets are enclosed by elastic membranes [20]. The membrane encapsulates the droplet content, which removes the surface tension effects and restricts topological changes. Therefore, studies on the compound capsules were mainly on their migrations, tumbling motions, and deformations in the ambient flow [21].

In the presence of substrates, the problem becomes more complicated due to a new factor involved: the wetting condition on solid boundaries. In some scenarios, the physical and chemical heterogeneities of the substance are considered, leading to the so-called contact-angle hysteresis [22]. This hysteresis contributes to a critical condition below which the droplet would pin to the substrate. Dimitrakopoulos and Higdon [23,24] employed the boundary element method to study the deformation of a droplet adhering to the solid surface in shear flow and the yield condition of droplet motion. Various surface properties and flow conditions were considered, yet the studies have been restricted to very low Reynolds numbers so that the creeping-flow theory can be used to facilitate analysis. Spelt [25] incorporated the inertial effect into the same problem by numerically resolving the Navier-Stokes equations at moderate Reynolds numbers. By considering the balance among forces exerted on the droplet, the scaling law between the critical Weber number of droplet motion and the Reynolds number was established. This work was followed by Ding and Spelt [26], who carried out three-dimensional simulations to enrich understandings in this problem. Other than studying the onset of motions, Ding *et al.* [27] also investigated the entrainment process and the pinch-off of droplets. An energy perspective was introduced to study the ligament dynamics, showing an exponential rate of stretching. In some other studies, a constant contact angle is assumed, due to which the droplet can move at any positive capillary number. With this assumption, Kang *et al.* [28] numerically investigated the droplet sliding in a duct under the action of gravity. It was found that the dimensionless contact-line velocity in sliding cases holds a linear relationship with the capillary number, indicating that a local balance is reached between the viscous force and the surface tension force. In this work, we will also employ the assumption of constant contact angles since our research interests lie in the kinematics and dynamics of the moving droplet rather than the onset of its sliding motion.

From the above reviews, we can see that existing research of the droplet dynamics on a substrate in shear flow was focused on the case of a single droplet. Although the laws and tendencies acquired in these studies are of reference value to the present investigation of a compound droplet, it is still necessary to make thorough kinematic and dynamic analyses on this configuration. We can only find very limited reports on this topic in the literature, most of which were dedicated to constructing robust numerical schemes for modeling ternary fluid systems with contact-line dynamics. Zhang *et al.* [29] proposed a diffuse-interface interpretation of the contact-line dynamics for a ternary fluid system based on the two-phase flow counterpart [30], and presented some preliminary results of the compound droplet on substrate in shear flow. Yu *et al.* [31] simulated this problem within the lattice Boltzmann framework and summarized several kinematic modes without further elaboration of the dynamics. Shang *et al.* [32] placed a smaller droplet into a larger one on the substrate and numerically studied the dynamics of the compound droplet in shear flow.

In this work, we would enrich understandings of this problem through numerical simulations. The lattice Boltzmann method (LBM) is an important numerical tool for resolving multiphase flow problems and has been widely employed in studying droplet dynamics [33–37]. However, the conventional LBM might be less competitive in memory cost and boundary treatment due to its evolution of distribution functions. The recently developed simplified lattice Boltzmann method (SLBM) [38], which directly evolves the macroscopic variables within the lattice Boltzmann framework, provides circumvention from these issues. To resolve the problem of interest in this work, we device a ternary phase-field simplified multiphase lattice Boltzmann method (TPF-SMLBM) in which the simplified multiphase lattice Boltzmann method [39] serves as the flow solver and the diffuse-interface model [29] resolved by SLBM evolves the interfaces. Compared with the conventional LBM, the present numerical strategy largely reduces the number of variables at each mesh point and thus lowers the consumption of virtual memory. In the meantime, both the physical boundary conditions and the wetting conditions on solid substrate can be directly implemented without tedious transformation into equivalent conditions for distribution functions.

Key physical questions to be answered from the numerical simulations include the kinematic modes, the triggering factors for the mode transitions, and typical flow dynamics in each mode. Specifically, three kinematic modes, namely the quasisteady sliding, tumbling-sliding, and tumbling-detachment, are recovered in our simulations. These modes are mostly in line with the previous work in a Poiseuille flow [31]. The pinch-off is not discussed here due to the difficulty in distinguishing the numerical pinch-off and the true physical breakup [40]. Dynamics of the quasisliding and the tumbling process will be established, following the paths of force and energy balances proposed by Dimitrakopoulos and Higdon [2] and Ding *et al.* [27]. An exponential shrinking rate of the wetted length in the early stage of evolution is mathematically derived, which agrees well with the simulation results. The onset dynamics of the tumbling motion will be physically explained from both the force balance point of view and the perspective of competing timescales, based on which the tumbling number $\mathrm{Tu} = \mathrm{Ca}/\mathrm{Re}^{-0.5}$ is defined to quantify the transition. This dimensionless parameter is justified through abundant numerical tests, and possesses the criticality of $O(1)$ upon onset of tumbling motion in the low-density–viscosity ratio scenarios considered here. Regarding the tumbling process, it is found that the re-adhesion of the tumbling droplet would generate extra diffusive flow behaviors and lead to the shrinking of wetted length of the droplet portion which always adheres to the substrate. Discussions of the detachment dynamics will be made mostly in a qualitative way. A scaling law of the critical capillary number of detachments $\mathrm{Ca}_{c,\mathrm{detach}} \sim \mathrm{Re}^{-0.3}$ is found based on the simulation results. Although a thorough mathematical derivation for this scaling law is difficult, given the extreme complexities involved in this process, it does imply that the viscous shear stress and surface tension force play a more dominant role in the detachment process comparing with the onset of tumbling. It should be stressed that the numerical studies in this work are carried out in low-density and viscosity ratio scenarios and in two-dimensional conditions. Although the physical insights from the findings in this work are of reference value to general applications, further verifications in three-dimensional simulations are expected. In the meantime, higher density and viscosity ratios could reveal more delicate physical phenomena and bring in more numerical challenges. Therefore, investigations in higher ratios of density and viscosity and three-dimensional simulations would certainly enrich the knowledge on this topic, which should be considered in our future work.

The remaining parts of the paper are organized as follows. Section II details the derivations and formulations of the TPF-SMLBM used in the simulations. The validity of the numerical method is established through two benchmark tests of ternary flow system in Sec. III. The validated method is employed in Sec. IV for comprehensive investigations of the compound droplet dynamics on substrate in shear flow. Concluding remarks are finally made in Sec. IV.

II. NUMERICAL METHOD

Numerical simulation of a ternary fluid system calls for robust multiphase flow solver and interfacial tracking algorithm. In this work, we will establish a TPF-SMLBM to fulfill these purposes. The

recently developed SMLBM will be employed as the flow solver [39], and the ternary phase-field model [29] will be resolved within the lattice Boltzmann framework to update the interface positions and interpret wetting conditions on the substrate.

A. Simplified multiphase lattice Boltzmann method as the flow solver

The LBM, being established at the mesoscopic scale, is a widely used numerical interpretation for the flow system. The popularity of LBM in the fluid mechanics community stems from its major advantages in kinetic nature, simplicity, and explicitness. LBM tracks the evolution of the so-called distribution functions f_α defined in the particle velocity space. To tackle the density discontinuity encountered in multiphase simulations, He *et al.* [41] fine-tuned the original LBM by introducing the incompressible transformation and proposed the following formulations for LBM resolution of the multiphase flow field:

$$f_\alpha(\mathbf{r}+\mathbf{e}_\alpha\delta_t, t+\delta_t) = f_\alpha(\mathbf{r},t) - \frac{f_\alpha(\mathbf{r},t) - f_\alpha^{eq}(\mathbf{r},t)}{\tau_v} + F_\alpha, \tag{1}$$

where $\mathbf{r}$ and t are, respectively, the space location and time level; the subscript α denotes the lattice velocity direction; $\mathbf{e}_\alpha$ is the lattice velocity vector; δ_t is the streaming time interval; τ_v represents the relaxation parameter and is related to the kinematic viscosity through $\nu = c_s^2\delta_t(\tau_v - 0.5)$, with c_s being the artificial sound speed; and F_α and f_α^{eq} are the forcing term and the equilibrium distribution function, which can be, respectively, expressed as

$$F_\alpha = \left(1 - \frac{1}{2\tau}\right)(\mathbf{e}_\alpha - \mathbf{u})\cdot[\Gamma_\alpha(\mathbf{u})(\mathbf{F}_s + \mathbf{G}) - (\Gamma_\alpha(\mathbf{u}) - \Gamma_\alpha(0))\nabla\psi(\rho)], \tag{2}$$

$$f_\alpha^{eq} = \rho c_s^2\Gamma_\alpha(\mathbf{u}) + \psi(\rho)\Gamma_\alpha(0), \tag{3}$$

with $\Gamma_\alpha(\mathbf{u}) = \omega_\alpha[1 + \frac{\mathbf{e}_\alpha\cdot\mathbf{u}}{c_s^2} + \frac{(\mathbf{e}_\alpha\cdot\mathbf{u})^2}{2c_s^4} - \frac{|\mathbf{u}|^2}{2c_s^2}]$ and $\psi(\rho) = p - \rho c_s^2$; ω_α is the weighting coefficient along a given lattice velocity direction α; ρ and $\mathbf{u}$ are the density and the velocity vector, respectively; and $\mathbf{F}_s$ and $\mathbf{G}$ denote the surface tension force and other external forces, respectively. The macroscopic variables can be obtained by $p = \sum_\alpha f_\alpha$ and $\rho\mathbf{u}c_s^2 = \sum_\alpha \mathbf{e}_\alpha f_\alpha$. In this work, the D2Q9 lattice velocity model is employed, which gives

$$\omega_\alpha = \begin{cases} 4/9, & \alpha = 0 \\ 1/9, & \alpha = 1\sim 4 \\ 1/36, & \alpha = 5\sim 8 \end{cases}, \tag{4}$$

$$\mathbf{e}_\alpha = c\begin{cases} (0,0), & \alpha = 0 \\ (\cos[(\alpha-1)\pi/2], \sin[(\alpha-1)\pi/2]), & \alpha = 1\sim 4 \\ (\cos[(2\alpha-9)\pi/4], \sin[(2\alpha-9)\pi/4]), & \alpha = 5\sim 8 \end{cases} \tag{5}$$

where $c = \delta_x/\delta_t$ is the lattice velocity scale and δ_x is the lattice length.

It is noteworthy that the direct evolution of the distribution function has brought high consumption of virtual memory and tedious transformation to the implementation of LBM in practical problems. To alleviate this issue, Chen and Shu [38] recently proposed a SLBM by directly evolving the macroscopic variables within the lattice Boltzmann framework and proved that the new method preserves good numerical stability. By extending this theory to the multiphase scenario, the SMLBM was developed [39]. The SMLBM starts from the macroscopic equations recovered from the above multiphase lattice Boltzmann equation (1) through the Chapman-Enskog expansion analysis and reconstructs the macroscopic solutions in the following predictor-corrector manner:

Predictor step:

$$p^* = \sum_\alpha f_\alpha^{eq\_m}(\mathbf{r} - \mathbf{e}_\alpha\delta_t, t - \delta_t), \tag{6}$$

$$\rho^*\mathbf{u}^*c_s^2 = \sum_\alpha \mathbf{e}_\alpha f_\alpha^{eq}(\mathbf{r} - \mathbf{e}_\alpha\delta_t, t - \delta_t). \tag{7}$$

Corrector step:

$$p(\mathbf{r},t)=p^{*}, \tag{8}$$

$$\rho(\mathbf{r},t)\mathbf{u}(\mathbf{r},t)c_s^2=\rho^{*}\mathbf{u}^{*}c_s^2+\sum_{\alpha}\mathbf{e}_{\alpha}\left[f_{\alpha}^{\sim}\left(\mathbf{r}+\frac{1}{2}\mathbf{e}_{\alpha}\delta_t,t-\frac{1}{2}\delta_t\right)-f_{\alpha}^{\sim}\left(\mathbf{r}-\frac{1}{2}\mathbf{e}_{\alpha}\delta_t,t-\frac{1}{2}\delta_t\right)\right]$$
$$-\frac{\delta_t}{2}\sum_{\alpha}\mathbf{e}_{\alpha}\left[F_{\alpha}^{\sim}\left(\mathbf{r}+\mathbf{e}_{\alpha}\delta_t,t-\frac{1}{2}\delta_t\right)-F_{\alpha}^{\sim}\left(\mathbf{r}-\mathbf{e}_{\alpha}\delta_t,t-\frac{1}{2}\delta_t\right)\right]+c_s^2(\mathbf{F}_s+\mathbf{G})\delta_t, \tag{9}$$

where the asterisk denotes the intermediate properties; $f_{\alpha}^{eq\_m}$ is calculated with Eq. (3) but utilizes the pressure values at the space and time levels of $(\mathbf{r},\mathrm{t}-\delta_t)$; and $F_{\alpha}^{\sim}=\tau_v F_{\alpha}$. And, the nonequilibrium term $f_{\alpha}^{\sim}$ is calculated by

$$f_{\alpha}^{\sim}\left(\mathbf{r}-\tfrac{1}{2}\mathbf{e}_{\alpha}\delta_t,t-\tfrac{1}{2}\delta_t\right)=\left[\tau_v\left(\mathbf{r}-\tfrac{1}{2}\mathbf{e}_{\alpha}\delta_t,t-\tfrac{1}{2}\delta_t\right)-1\right]\left[f_{\alpha}^{eq}(\mathbf{r},t)-f_{\alpha}^{eq}(\mathbf{r}-\mathbf{e}_{\alpha}\delta_t,t-\delta_t)\right]. \tag{10}$$

Detailed derivations of the above SMLBM formulations (6)–(9) can be found in Ref. [39]. The SMLBM preserves some distinct advantages due to its direct evolution of macroscopic variables. The distribution functions are no longer stored in computations, which reduces the memory cost. In the meantime, the physical boundary conditions for the macroscopic variables can be directly implemented without further transformations.

B. Ternary phase-field method as the interface tracking algorithm

1. Ternary phase-field model and lattice Boltzmann equation

As a typical Eulerian scheme, the SMLBM requires extra algorithms to update the interfaces between different phases. The phase-field method has demonstrated its flexibility in describing complex interfaces and thus has been attracting increasing attention in the community of multiphase simulation. In this work, we consider the following Cahn-Hilliard equation for a ternary fluid system [42]:

$$\frac{\partial\varphi_i}{\partial t}+\nabla\cdot(\mathbf{u}\varphi_i)=\nabla\cdot(M_i\nabla\mu_i), \tag{11}$$

where φ is the order parameter; the subscript i denotes the ith phase; $M_i=M_0/\lambda_i$ is the mobility, with M_0 being a constant diffusive parameter; $\mathbf{u}$ is the velocity vector; and $\lambda_i=\sigma_{ij}+\sigma_{ik}-\sigma_{jk}$ is a parameter that is related to the surface tensions between different phases, with σ_{ij} representing the surface tension between phase i and phase j. The order parameter fulfills the constraint of $\sum_{i=1}^{3}\varphi_i=1$. And, from the formula of bulk energy proposed by Boyer and Lapuerta [42], the chemical potential μ is obtained by

$$\mu_i=\frac{12}{\xi}[\lambda_i\varphi_i(1-\varphi_i)(1-2\varphi_i)-\delta\varphi_1\varphi_2\varphi_3]-\frac{3}{4}\xi\lambda_i\nabla^2\varphi_i, \tag{12}$$

with $\delta=6\lambda_1\lambda_2\lambda_3/(\lambda_1\lambda_2+\lambda_1\lambda_3+\lambda_2\lambda_3)$ and ξ being the interface thickness.

In the presence of a solid substrate which is assumed to be smooth and chemically homogeneous, a static contact angle θ can be used to quantify the wettability of the substrate. The value of the contact angle is commonly associated with the surface tension through the Young equation $\cos\theta_{ij}=(\sigma_{js}-\sigma_{is})/\sigma_{ij}$, where subscripts i and j represent the liquid phases, and the subscript s denotes the substrate. The contact angle can be numerically interpreted by either a geometric way or the energy point of view. Ding and Spelt [30] demonstrated that these two interpretations can be equally transformed. In the present implementation in a ternary fluid system, the geometric wetting condition proposed by Zhang *et al.* [29] is used, which gives

$$\mathbf{n}\cdot\nabla\varphi_i=-\tan\left(\frac{\pi}{2}-\theta_i\right)|\nabla\varphi_i-(\mathbf{n}\cdot\nabla\varphi_i)\mathbf{n}|, \tag{13}$$

where θ_i denotes the weighted contact angle of liquid phase i in the presence of solid substrate and is calculated by

$$\theta_i = \frac{\varphi_j}{\varphi_j + \varphi_k}\theta_{ij} + \frac{\varphi_k}{\varphi_j + \varphi_k}\theta_{ik}. \tag{14}$$

Referring to the work of Huang *et al.* [43] for binary flow system, the following lattice Boltzmann equation is tailored to equivalently express the above macroscopic equations (11) for ternary interface tracking:

$$h_\alpha^i(\mathbf{r} + \mathbf{e}_\alpha \delta_t,\ t + \delta_t) = h_\alpha^i(\mathbf{r},\ t) - \frac{h_\alpha^i(\mathbf{r},\ t) - h_\alpha^{i,eq}(\mathbf{r},\ t)}{\tau_i}, \tag{15}$$

where h is the distribution function for the order parameter; τ_i is the relaxation parameter for the order parameter of the ith phase and is related to the mobility by

$$\frac{M_0}{\lambda_i} = (\tau_i - 0.5)\eta\delta_t. \tag{16}$$

Here η is a diffusion parameter. The equilibrium distribution function reads

$$h_\alpha^{i,eq} = \begin{cases} \varphi_i - \mu_i\eta(1-\omega_0)/c_s^2, & \alpha = 0 \\ \omega_\alpha(\mu_i\eta + \varphi_i \mathbf{e}_\alpha \cdot \mathbf{u})/c_s^2, & \alpha = 1-8 \end{cases}. \tag{17}$$

The consistency between the lattice Boltzmann equation (15) and the macroscopic equation (11) can be established through the Chapman-Enskog expansion analysis, which is detailed in Appendix A.

2. Numerical resolution

To maintain consistency with the numerical strategies of flow solver, the order parameters will be resolved by the theory of SLBM [38]. With detailed derivations presented in Appendix B, the following evolution equations for the order parameter can be obtained.

Predictor step:

$$\varphi_i^* = \sum_\alpha h_\alpha^{i,eq}(\mathbf{r} - \mathbf{e}_\alpha\delta_t,\ t - \delta_t). \tag{18}$$

Corrector step:

$$\varphi_i(\mathbf{r},\ t) = \varphi_i^* + \sum_\alpha (\tau_i - 1)\left[h_\alpha^{i,\sim}\left(\mathbf{r} + \frac{1}{2}\mathbf{e}_\alpha\delta_t,\ t - \frac{1}{2}\delta_t\right) - h_\alpha^{i,\sim}\left(\mathbf{r} - \frac{1}{2}\mathbf{e}_\alpha\delta_t,\ t - \frac{1}{2}\delta_t\right)\right], \tag{19}$$

where the nonequilibrium term is evaluated by

$$h_\alpha^{i,\sim}\left(\mathbf{r} - \tfrac{1}{2}\mathbf{e}_\alpha\delta_t, t - \tfrac{1}{2}\delta_t\right) = \left[\tau_i\left(\mathbf{r} - \tfrac{1}{2}\mathbf{e}_\alpha\delta_t, t - \tfrac{1}{2}\delta_t\right) - 1\right]\left[h_\alpha^{i,eq}(\mathbf{r}, t) - h_\alpha^{i,eq}(\mathbf{r} - \mathbf{e}_\alpha\delta_t, t - \delta_t)\right]. \tag{20}$$

The evolved order parameters are utilized to update the fluid density and other parameters through $\zeta = \sum_{i=1}^{3}\varphi_i\zeta_i$, where ζ is a placeholder for density ρ, kinematic viscosity ν, and relaxation parameter τ. In practice, we only need to resolve two order parameters, and the remaining one can be evaluated by the unity condition $\sum_{i=1}^{3}\varphi_i = 1$.

A clear merit brought by using evolution formulations (18) and (19) instead of Eq. (17) is that it allows direct implementation of the boundary conditions for the order parameter. Specifically, the space derivatives in the boundary condition formulation (13) are approximated by one-sideite difference scheme with the second order of accuracy. Moreover, without updating and storing the distribution functions h, the number of interface-tracking related variables at each mesh point is reduced from 18 to 2 when using the D2Q9 lattice velocity model, which indicates significant reduction in memory cost.

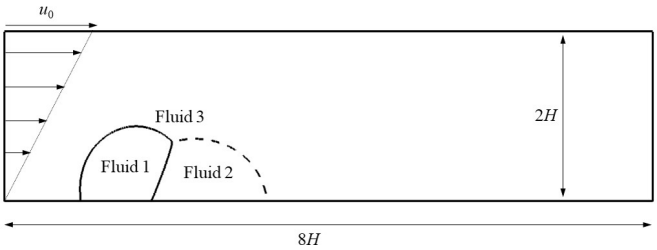

FIG. 1. Schematic diagram of a compound droplet placed on a substrate in a shear flow.

C. Numerical validations

Before employing the proposed method in studying the problem of interest, it is necessary to validate its accuracy and robustness. To maintain compactness of this paper, we relocate the validation to Appendix C, in which two numerical examples will be presented for validation purposes.

III. APPLICATION TO COMPOUND DROPLET DYNAMICS ON SOLID SURFACE IN SHEAR FLOW

A. Problem statement

The schematic diagram of the problem is illustrated in Fig. 1. The flow system includes three fluid phases. The compound droplet with the initial radius of H consists of two equal portions of fluid 1 and fluid 2, while the ambient flow current belongs to fluid 3. The surface tensions and contact angles between different phases are collectively written as σ_{ij} and θ_{ij}, respectively, where subscripts i and j denote the indices of fluid phases. Without specific statements, the present work considers equal surface tensions between different phases, and the contact angles are set as $\theta_{12} = 120^\circ$, $\theta_{13} = 90^\circ$, and $\theta_{23} = 60^\circ$. The height of the channel is $2H$, and the top lid is moving at a constant velocity u_0 which generates a shear rate of $\dot{\gamma} = u_0/2H$. The computational domain has the length of $8H$. The left and the right boundaries are periodic, while the top wall fulfills the no-slip boundary condition. Although the slip length could have influence of the droplet motion on the substrate, we still assume the bottom wall to be no slip (zero slip length). The effect of slip length is left for future studies, due to the limit of article length here. In numerical simulations, we carry out the preprocessing as per suggestions of Zhang *et al.* [29]. The compound droplet is initially placed on the substrate with no ambient flow current and gradually reaches an equilibrium shape. A linear velocity profile is then implemented on fluid 3 at the dimensionless time marked as T=0, after which the shear rate is maintained by imposing constant velocity on the top wall. We emphasize that this work concerns the sliding droplets and therefore neglects the contact-angle hysteresis.

By utilizing the properties of H, $\dot{\gamma}H$, and $1/\dot{\gamma}$ as the scales of length, velocity, and time, respectively, the dimensionless parameters of Reynolds number (Re), capillary number (Ca), Weber number (We), and Ohnesorge number (Oh) can be defined as

$$\mathrm{Re} = \frac{\rho_1 \dot{\gamma} H^2}{\mu_1}, \tag{21}$$

$$\mathrm{Ca} = \frac{\mu_1 \dot{\gamma} H}{\sigma_{12}}, \tag{22}$$

$$\mathrm{We} = \mathrm{Ca} \cdot \mathrm{Re} = \frac{\rho_1 \dot{\gamma}^2 H^3}{\sigma_{12}}, \tag{23}$$

$$\mathrm{Oh} = \frac{\sqrt{\mathrm{We}}}{\mathrm{Re}} = \frac{\mu_1}{\sqrt{\rho_1 \sigma_{12} H}}, \tag{24}$$

TABLE I. Parametric settings of density and viscosity ratios in simulation cases.

	Density ratio	Viscosity ratio
Case series 1	1:1.1:0.8	1:0.66:1.6
Case series 2	1:1:1	1:1:1
Case series 3	1:0.9:0.8	1:1.36:1.6

where ρ and μ are the fluid density and dynamic viscosity, respectively. The above dimensionless parameters are based on fluid properties of fluid 1. Fluid properties of other fluid phases are obtained by the specified ratios of density and viscosity. In the present work, we have carried out three sets of tests as shown in Table I to illustrate the applicability of the conclusions in small density–viscosity ratio scenarios. Further investigations in larger density and viscosity ratios will be considered in future studies. The contact-angle hysteresis is neglected, meaning that the contact angle would be a constant value for a given fluid. To circumvent the discussion of turbulence, which is not among the present research interests, the Reynolds numbers in simulations are in the moderate range of 10 to 100. And, for each Reynolds number, simulations of cases at different capillary numbers will be performed. For clarity, the interval of the capillary number in our numerical cases is 0.01.

B. Grid independence

To determine the appropriate mesh size to be used in the numerical investigation, we firstly perform grid independence study. Two mesh sizes, namely 801 $\times$ 201 and 1601 $\times$ 401, are used in the tests. The interface locations are shown in Fig. 2, indicating that converged results can be obtained on the mesh size of 801 $\times$ 201. Therefore, the following computations will be carried out on this mesh size.

C. Results

1. Kinematic modes

Forces exerted on the compound droplet placed in the shear flow include the form drag, the shear stress, and the surface tension. Delicate balance among these forces would result in various flow phenomena. A general tendency is that, by increasing either the Reynolds number or the capillary

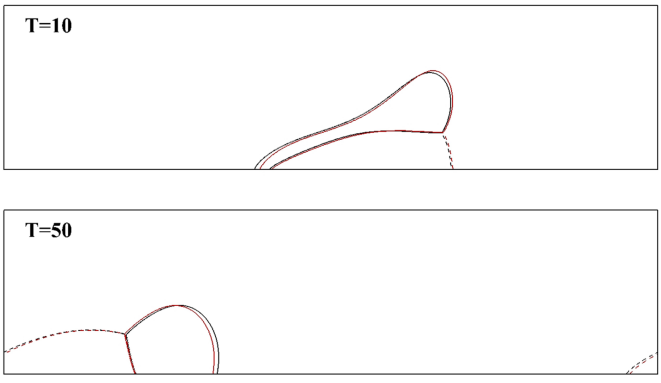

FIG. 2. Grid-independence tests at equal density and viscosity ratios with Re=50 and Ca=0.10. The black and the red curves represent the results obtained on mesh sizes of 801 $\times$ 201 and 1601 $\times$ 401, respectively. The solid and the dashed lines are interface locations of fluid 1 and fluid 2, respectively. Note that the left and the right boundaries of the computational domain are periodic.

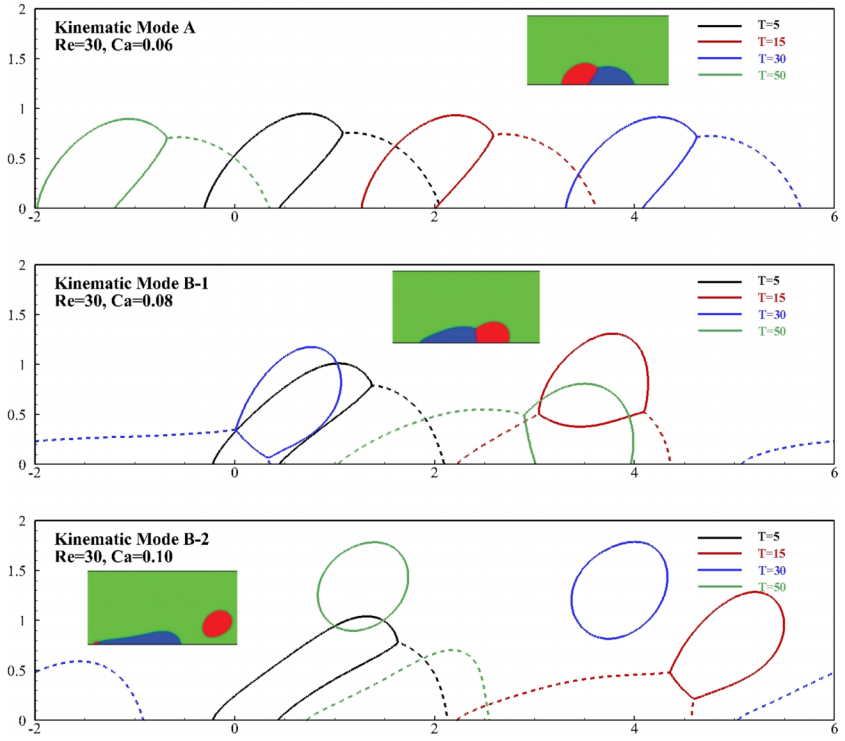

FIG. 3. Illustration of three kinematic modes for a compound droplet moving in the shear flow. Presented in each subfigure are interface locations at dimensionless time of T=5 (black lines), 15 (red lines), 30 (blue lines), and 50 (green lines). The solid lines represent the interface location of fluid 1, and the dashed lines depict the interface of fluid 2. Simulation results are from case series 1. Note that the channel is periodic on its left and right boundaries. The reference kinematic modes from Ref. [31] are also included as the small window figures for comparison.

number, larger deformation of the compound droplet can be expected. This is in line with the physical deduction that the form drag and viscous shear stress from ambient fluid contribute to the deformation of droplet, while the surface tension and wall shear stress obstruct this process. In our simulations, three typical kinematic modes have been recovered: the quasisteady sliding mode, the tumbling-sliding mode, and the tumbling-detachment mode. Specifically, the quasisteady sliding mode refers to the cases in which the compound droplet would slightly deform without switching the relative location of its two fluid portions and then slide on the substrate in a roughly constant speed. The tumbling motion of the compound droplet may occur in higher Reynolds or capillary numbers, which is identified by the switching between the relative location of two fluid portions of the droplet. By further increasing the Reynolds or the capillary numbers, the droplet portion of fluid 1 could detach from the portion of fluid 2 during its tumbling motion. For the ease of analysis, we term the quasisliding mode as mode A, the tumbling-sliding mode as mode B-1, and the tumbling-detachment mode as mode B-2, which are illustrated in Fig. 3. Although these kinematic modes of a compound droplet in shear flow have been reported in the literature (see the small figures extracted from Ref. [31]), associated dynamic analyses are limited. In Secs. III C 2–III C 5, endeavors will be made to establish physical rational for each kinematic mode and the transition dynamics.

It should be noted that the kinematic modes of a compound droplet could also be related to the contact angles of the composed fluids. In the range of Reynolds numbers investigated here,

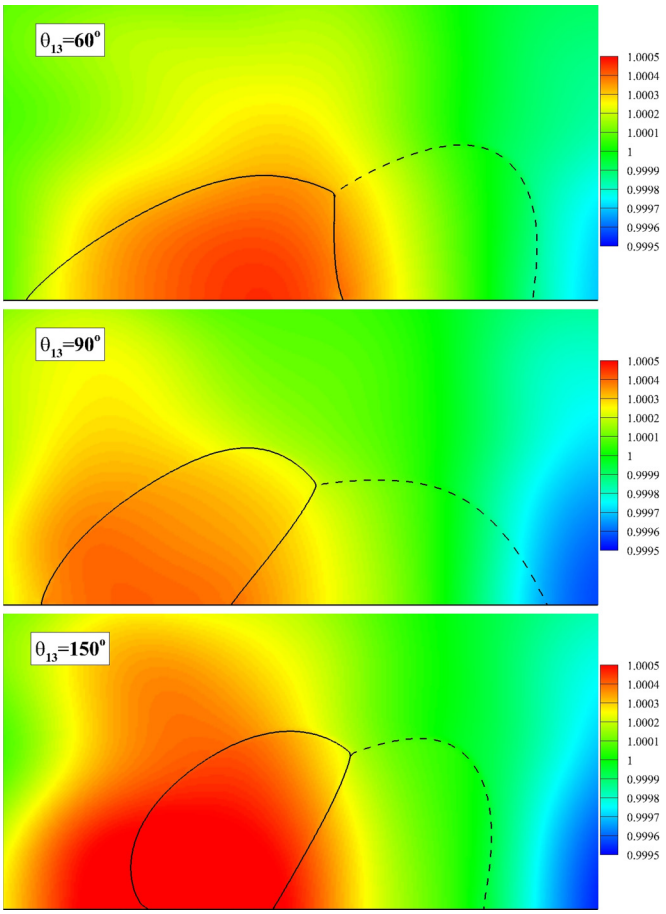

FIG. 4. Pressure contours and interface locations at dimensionless time T=1 for cases with different contact angles of $\theta_{13} = 60^\circ$ (top), 90° (middle), and 150° (bottom). Density and viscosity ratios are both 1:1:1. Re=50, Ca=0.10.

we found that a key factor to trigger the tumbling motion is the contact angle between the front fluid portion of the droplet and the ambient fluid, namely the contact angle θ_{13} between fluid 1 and fluid 3 in Fig. 1. For illustration purposes, we consider equal ratios of density and viscosity, and present results in three sets of contact angles of $(\theta_{13}, \theta_{12}, \theta_{23}) = (90^\circ, 120^\circ, 60^\circ)$, $(60^\circ, 60^\circ, 90^\circ)$, and $(150^\circ, 120^\circ, 90^\circ)$. As shown in Fig. 4, if the contact angle θ_{13} is smaller than 90°, no tumbling motion would happen, and the compound droplet only exhibits larger deformation at higher Reynolds or capillary numbers. A preliminary explanation for this phenomenon is that a nonacute contact angle θ_{13} may contribute to the form drag exerted from the ambient fluid to the compound droplet, especially in the frontal part, which provides necessary torque to the tumbling motion towards the downstream. With an acute contact angle θ_{13}, the droplet is more easily deformed into a streamline shape under the action of form drag. Such response quickly dissolves effect of the form drag, and thus leads to insufficient torque to trigger the tumbling motion. The reduced form drag can be qualitatively demonstrated by the smaller high-pressure region in the frontal area of the droplet, as shown in Fig. 4. To avoid overspreading of the discussions, here we only study the configuration which can lead to the tumbling motion, based on which detailed dynamics will be investigated. As stated before, the contact angles used in the following simulations are $\theta_{12} = 120^\circ$, $\theta_{13} = 90^\circ$, and $\theta_{23} = 60^\circ$.

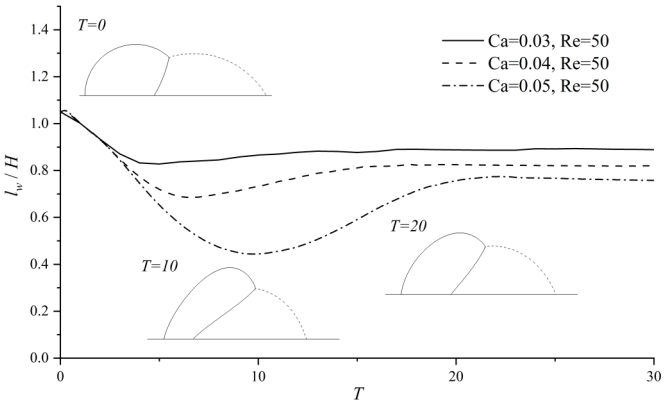

FIG. 5. Time histories of the wetted length on the substrate for the droplet portion of fluid 1 at Re = 50. Data are collected in case series 1. Inserted interface locations are for the case of Re = 50 and Ca = 0.05 at two dimensionless time of T=10 and 20.

2. Quasisteady sliding

For the configuration investigated in this work, the compound droplet exhibits quasisteady sliding either at lower Reynolds numbers for a given capillary number or at smaller capillary numbers when the Reynolds number remains unchanged. The former scenario implies that the form drag contributes to the deformation of the droplet. The latter case suggests that the surface tension force helps the droplet to adhere to the substrate, while the viscous stress from the ambient fluid could be benefiting to the deformation or even the tumbling of the droplet.

By looking into the evolution of the wetted length (l_w) for the sliding cases considered here, we can investigate the response of the droplet to the forces exerted by ambient fluid. As illustrated in Fig. 5, it is found that the wetted length would be shrinking in early stage of evolution, and then expand until reaching the steady state. Intuitively, the initial shrinking of the wetted length of droplet portion of fluid 1 results from both the pressing from the ambient fluid on the frontal part of the droplet and the initially stationary droplet portion of fluid 2. This early stage of evolution can be physically interpreted as that the force exerted from the surrounding fluid is partially converted into the surface energy. This interpretation has been utilized by Ding *et al.* [27] in studying the ligament dynamics of a pinned droplet stretching in shear flows and can be mathematically expressed as

$$\sigma \frac{d}{dt} S_i \sim \int_{S_i} \mathbf{n} \cdot \mathbf{T} \cdot \mathbf{u} dS, \tag{25}$$

where S_i is the interface length; $\mathbf{T}$ is the stress tensor; and $\mathbf{n}$ is the unit normal vector pointing outward from the droplet surface. The interface length refers to the length of interface shared with other fluids, which is tentatively scaled as $S_i \sim H^2/l_w$. The remaining terms on the right-hand side of Eq. (25) are scaled as $\mathbf{T} \sim \mu\dot{\gamma}$ and $\mathbf{u} \sim \dot{\gamma}H$. After substitution, the following relationship can be derived:

$$-\frac{1}{l_w/H} \frac{d(l_w/H)}{d(\dot{\gamma}t)} \sim \frac{\mu\dot{\gamma}H}{\sigma} = \mathrm{Ca}. \tag{26}$$

Note that l_w/H and $\dot{\gamma}t$ represent the dimensionless wetted length and the dimensionless time, respectively. Equation (26) indicates an exponential evolution rate of the wetted length in the early shrinking stage, and the shrinking rate would be amplified by enlarging the capillary number. These implications are well supported by the numerical results shown in Fig. 5.

The subsequent expansion stage of evolution can be explained in a similar manner as that the accumulated surface energy is partially released and absorbed by ambient fluid through viscous

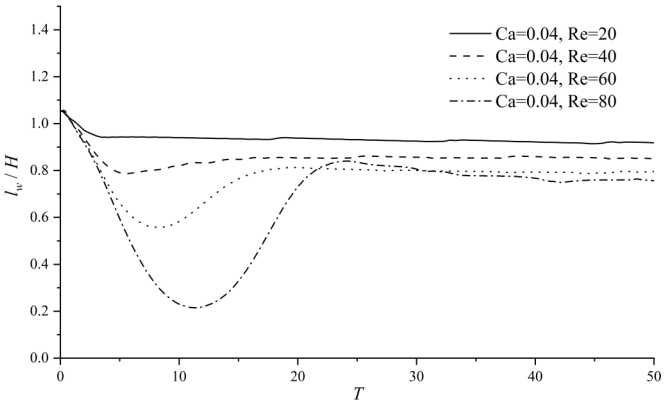

FIG. 6. Time histories of the wetted length on the substrate for the droplet portion of fluid 1 at Ca=0.04. Data are collected in case series 1.

diffusion, which is mathematically expressed as

$$\sigma \frac{d}{dt} S_i \sim -\int_{S_i} \mathbf{n} \cdot \mathbf{T} \cdot \mathbf{u} dS. \tag{27}$$

Note that Eq. (27) has a negative mark on the right-hand side to reflect the diffusive behavior. Other than that, all terms can be scaled in the same way as for the above analyses of Eq. (25). Through simple manipulations, we have

$$\frac{1}{l_w/H} \frac{d(l_w/H)}{d(\dot{\gamma} t)} \sim \mathrm{Ca}. \tag{28}$$

The above relation explains the exponential growth rate, which is also positively related to the capillary number, in the expansion stage of the wetted line evolution.

At a fixed capillary number, the amplitude of the initial shrinking of the wetted line could be enlarged by increasing the Reynolds number, as shown in Fig. 6. This can be explained by the lower physical viscosity at larger Reynolds number, due to which less portion of energy input from ambient fluid is diffused and thus more is converted into the surface energy.

After reaching the stage of quasisteady sliding, the compound droplet would maintain an equilibrium shape and move in a constant speed. This is characterized by a roughly constant contact-line speed V_c . Note that V_c is numerically calculated by the central difference scheme from the recorded contact-line locations at different time. By ignoring the contact-angle hysteresis, the sliding speed results from the balance between the viscous drag exerted from ambient fluid and the wall stress when moving the droplet on the substrate [27]. As reported in Kang *et al.* [28], the equilibrium contact-line speed would only be related to the capillary number Ca for a droplet sliding in quasisteady state, given the same shear rate. This relation should also be valid here if we neglect the interaction among different portions of the compound droplet and consider it as a whole droplet. Numerical examples in Fig. 7 validate that, for a given capillary number, the contact-line speeds would converge to roughly the same value in cases with different Reynolds numbers. The linear relation between the dimensionless contact-line speed $\mathrm{Ca}_{cl} = \mu V_c/\sigma$ and the capillary number, which was initially proposed by Kang *et al.* [28], is also recovered in the present tests over the moderate range of Reynolds numbers. A series of test results is presented in Fig. 8. The linearly fitted line would intersect with the x coordinate in a positive value of capillary number, indicating that this linear relation may not hold true in small capillary number scenario where the surface tension effect dominates.

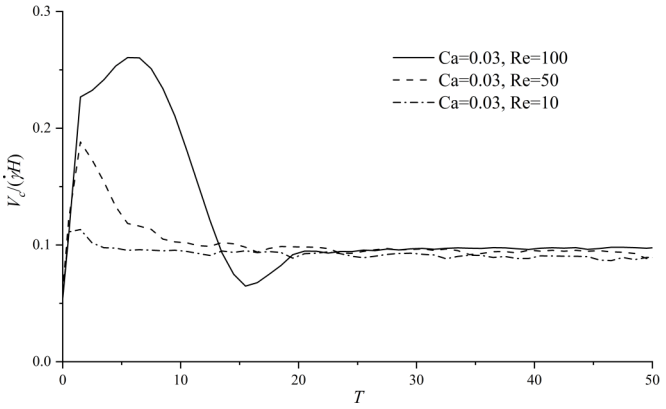

FIG. 7. Evolution of the upstream contact-line velocity of the droplet portion of fluid 1 in quasisteady sliding mode for some typical examples in case series 1.

Now we briefly illustrate the flow patterns for some typical quasisteady sliding cases. Figure 9 illustrates cases at the fixed Reynolds number of 50 and with different capillary numbers, while Fig. 10 shows the results at the same capillary number of 0.03 but with different Reynolds numbers. Note that the volume-averaged sliding velocity of the compound droplet has been deducted from the velocity field, based on which the stream function and the vorticity are numerically calculated using the central difference scheme. It is also noteworthy that the occasional penetration of streamlines through the boundary of two droplet portions is due to the numerical errors in postprocessing. From these two sets of figures, we can see that the droplet is more deformed in higher Reynolds or capillary numbers. Larger Reynolds number suggests reduced viscous effects and therefore fewer diffusivities. More energy input from the ambient fluid can be converted into the surface energy of the droplet, which is characterized by the larger deformation of the droplet. Larger capillary number means less obstruction exerted by the surface tension force, which also contributes to the deformation of compound droplet. In the meantime, the steadily sliding droplet consists of four major recirculation zones distributed along the streamwise direction: one locating in front of the compound droplet, another attached to the rear of it, and each droplet portion includes a major vortex rotating along the clockwise direction. The separated vortices in the two droplet portions lead to more abrupt velocity changes near the interfacial regions. Larger vorticities are observed in

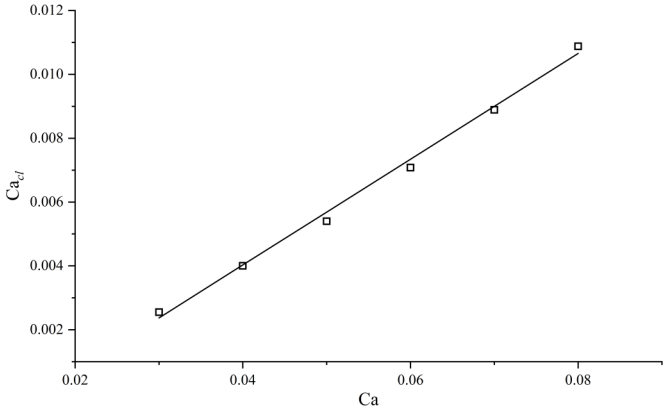

FIG. 8. Dimensionless contact-line speed Ca_{cl} as a function of the capillary number Ca for cases at Re=15. Data are collected in test series 1.

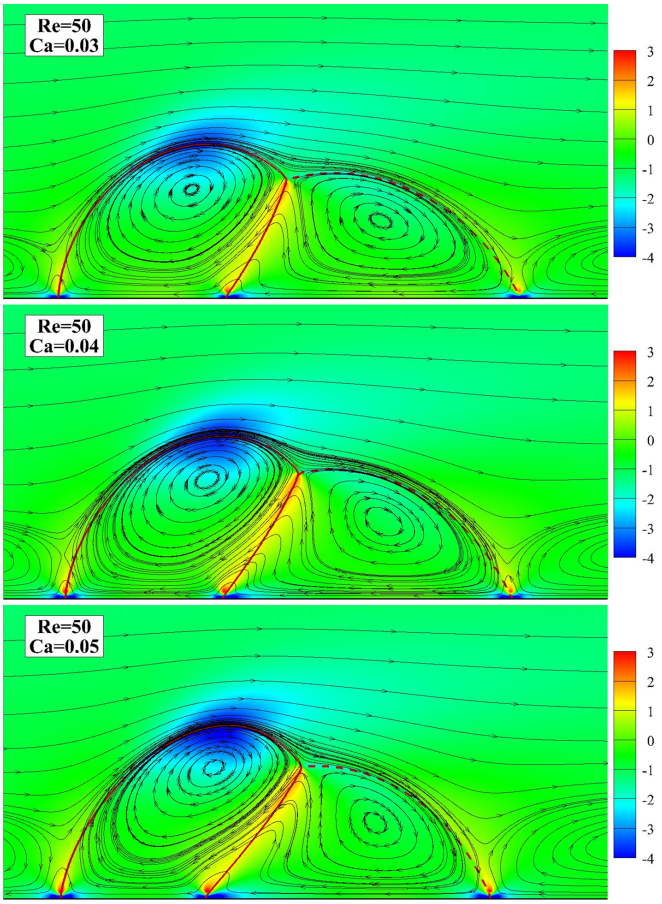

FIG. 9. Vorticity contours and streamlines at Re=50 and with different capillary numbers of Ca=0.03 (top), 0.04 (middle), and 0.05 (bottom). Results are from case series 1.

cases with higher Reynolds or capillary numbers, indicating stronger shear stress in these conditions. Similar tendencies have also been witnessed in other case series with different density and viscosity ratios, although the flow details could be different from the presented ones at the same Reynolds and capillary numbers.

3. Onset dynamics of tumbling motion

For a given Reynolds number, in cases with relatively lower capillary numbers, the compound droplet adheres to the substrate and slides in a quasisteady mode. In such circumstances, a force balance is achieved among the form drag, viscous force, and surface tension force [25]. A scaling argument, which is similar to the argument made in Ref. [25], can thus be established here. The form drag is approximated by $\alpha_f \rho_1 H(\dot{\gamma} H - V_s)^2$, with V_s being the sliding velocity of the droplet; the viscous force consists of the viscous component exerted by the fluid and the integrated wall shear stress, which are, respectively, written as $\alpha_v \mu_1 H \dot{\gamma}$ and $\alpha_w \mu_1 V_s$; and the net surface tension force posed on the droplet of fluid 1 can be tentatively expressed as $\sigma_{13} \cos\theta_{13} - \sigma_{12} \cos\theta_{12}$. Here, α_f, α_v, and α_w are unknown parameters. The force balance results in

$$\sigma_{13} \cos\theta_{13} - \sigma_{12} \cos\theta_{12} = \alpha_v \mu_1 H \dot{\gamma} + \alpha_w \mu_1 V_s + \alpha_f \rho_1 H(\dot{\gamma} H - V_s)^2, \tag{29}$$

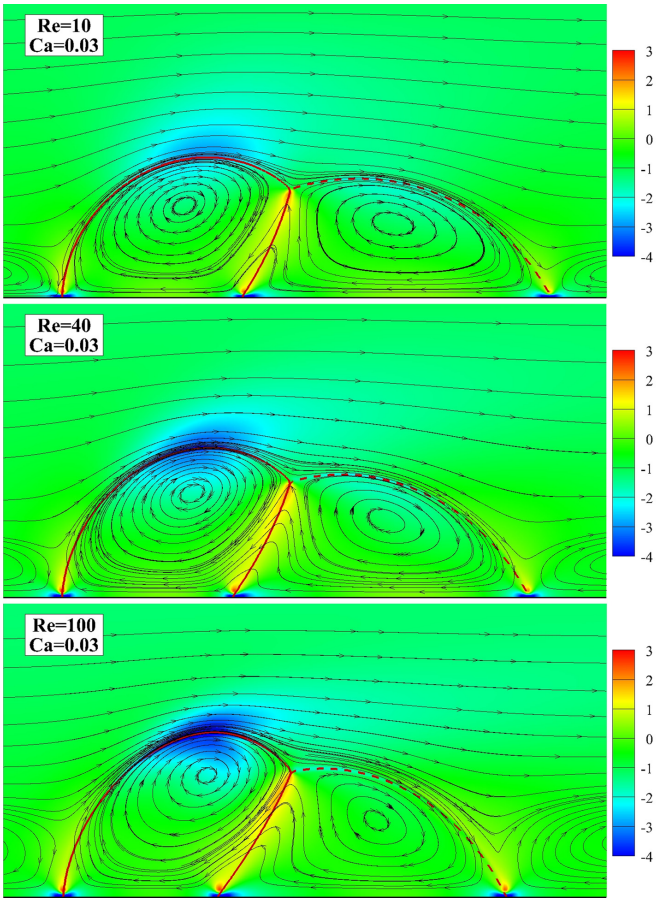

FIG. 10. Vorticity contours and streamlines at Ca=0.03 and with different Reynolds numbers of Re=10 (top), 40 (middle), and 100 (bottom). Results are from case series 1.

which derives

$$(\sigma_{13}\cos\theta_{13}-\sigma_{12}\cos\theta_{12})/\sigma_{12}=\alpha_f \mathrm{ReCa}\left(1-\frac{\mathrm{Ca}_s}{\mathrm{Ca}}\right)^2+\left(\alpha_v+\alpha_w\frac{\mathrm{Ca}_s}{\mathrm{Ca}}\right)\mathrm{Ca}, \tag{30}$$

where $\mathrm{Ca}_s=\mu_1 V_s/\sigma$. In quasisteady sliding cases, the sliding velocity V_s of the compound droplet should be equal to the moving velocity V_c of the contact line. With the linear relationship between the dimensionless contact-line velocity and the capillary number proposed by Kang *et al.* [28], we tentatively write $\mathrm{Ca}_s/Ca=b$, and the above Eq. (30) becomes

$$\mathrm{Ca}=\frac{(\sigma_{13}\cos\theta_{13}-\sigma_{12}\cos\theta_{12})/\sigma_{12}}{(\alpha_v+\alpha_w b)+\alpha_f(1-b)^2\mathrm{Re}}. \tag{31}$$

The above formulation establishes the relationship between the capillary number and the Reynolds number for quasisteady sliding motion. The numerator is a constant which is dependent on the fluid properties of the compound droplet; the denominator consists of two unknowns, namely $(\alpha_v+\alpha_w b)$ and $\alpha_f(1-b)^2$, which can be dependent on particular cases. The physical significance of this formulation is that it is a set of curves on which the sliding motion dynamics should be fulfilled. It also suggests that the violation of this relationship could imply the collapse of the quasisteady sliding motion and the transition towards other kinematic modes. In this sense, the

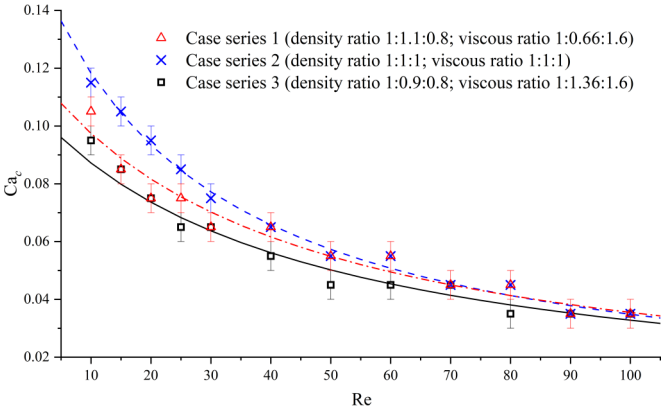

FIG. 11. Critical capillary number for the onset of tumbling mode as a function of Reynolds number.

critical capillary number, which identifies the transition from the quasisteady sliding to the tumbling motion mode, should be represented by this formulation. With the surface tension coefficients and contact angles used in our modelings, the numerator of Eq. (31) reads 0.5. The unknown coefficients can be determined by curve fitting based on the critical capillary number Ca_c obtained at each Reynolds number, which gives $[\alpha_v + \alpha_w b, \alpha_f(1-b)^2] = (4.1376, 0.0995)$, (3.1047, 0.1124), and (4.6774, 0.1057) for the three case series considered, as shown in Fig. 11. Note that the accurate value of Ca_c cannot be truly obtained due to the finite intervals selected in simulations. Therefore, it is bounded by the error bar with the upper limit given by the lowest capillary number which gives the kinematic mode B and the lower limit given by the highest capillary number which leads to the kinematic model A.

Apart from the above analysis based on the force balance along the x direction, another approach of dynamic analysis can be established by considering the magnitude of force balance. Similar to the previous scaling analysis, the drag force, the viscous shear force, and the surface tension can be, respectively, scaled as $\rho_1 H^3 \dot{\gamma}^2$, $\mu_1 H \dot{\gamma}$, and σ_{12}. The tumbling motion of the droplet portion of fluid 1 along the clockwise direction is stimulated by the coordinative effects of the viscous shear force and the form drag, and is obstructed by the surface tension. Therefore, following the definition of Ohnesorge number which describes the ratio of viscous force to the geometric mean magnitude of the inertial and surface tension forces, we define the following dimensionless parameter, which is tentatively called "tumbling number," to quantify the balance of the magnitudes of forces:

$$\mathrm{Tu} = \frac{\sqrt{\text{form drag} \cdot \text{viscous force}}}{\text{surface tension}} = \frac{\sqrt{(\rho_1 \dot{\gamma}^2 H^3)(\mu_1 \dot{\gamma} H)}}{\sigma_{12}} = \frac{\mathrm{Ca}}{\mathrm{Re}^{-0.5}}. \tag{32}$$

A slightly different parameter of $\mathrm{G} = \mathrm{Ca}^2/\mathrm{Re}$ has been proposed in Seevaratnam *et al.*'s [44] experiments to assist distinguishing different kinematic modes of a pure droplet on solid substrate in a shear flow. Other than its difference from the proposed tumbling number in formulations, no compact scaling laws were established in Seevaratnam *et al.*'s [44] work to describe the mode transition; neither was robust physical interpretation offered for the dimensionless parameter G.

To test the effectiveness of the parameter Tu in justifying the tumbling dynamics of droplet portion of fluid 1, we plot the phase diagrams of the kinematic modes of cases at different capillary and Reynolds numbers in Figs. 12–14. Being presented in log scale, the quasisteady sliding cases in kinematic mode A can roughly be separated from other tumbling cases in kinematic modes B-1 or B-2 by a straight line with the slope of $k = -0.5$, which fulfills the relationship established in Eq. (32).

To enrich the physical rational of the proposed dimensionless parameter Tu, we now consider another interpretation from the perspective of timescales. This approach has been utilized to analyze

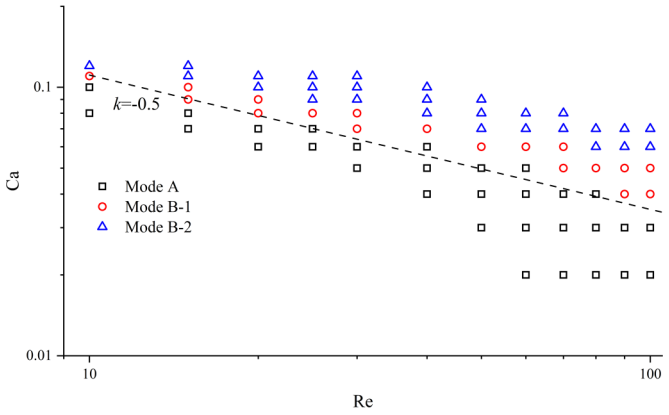

FIG. 12. Phase diagram of kinematic modes for case series 1. The coordinates are capillary and Reynolds numbers in log scale.

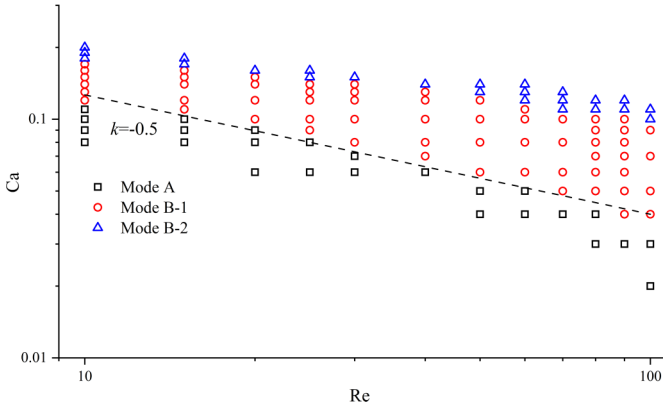

FIG. 13. Phase diagram of kinematic modes for case series 2. The coordinates are capillary and Reynolds numbers in log scale.

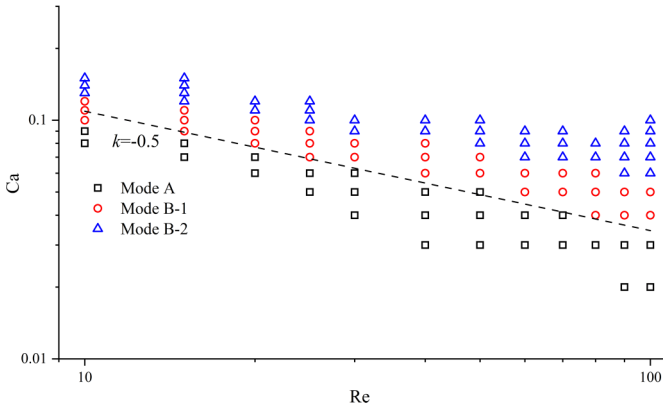

FIG. 14. Phase diagram of kinematic modes for case series 3. The coordinates are capillary and Reynolds numbers in log scale.

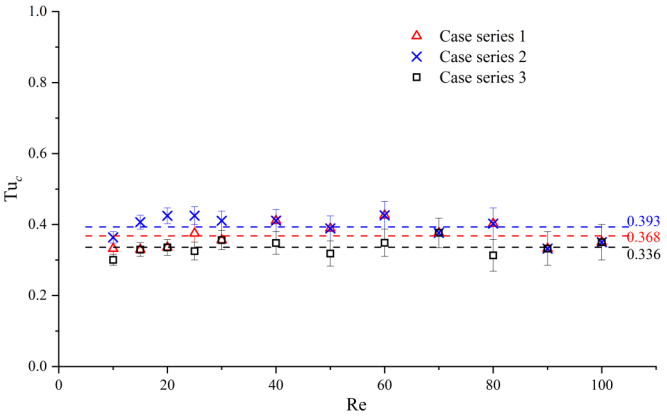

FIG. 15. Critical tumbling numbers at each Reynolds number for all case series. The values of averaged critical tumbling numbers are attached at the end of fitted lines. The upper limit of the error bar is the lowest tumbling number for the tumbling mode, while the lower limit of the error bar represents the highest tumbling number for the quasisliding mode.

the pinch-off of liquid threads [45] as well as to physically interpret the Ohnesorge number [46]. For the present configuration, the driving forces of the tumbling motion of the droplet portion of fluid 1 include the form drag and the net viscous force which is the shear force from ambient fluid subtracted by the shear stress force on the substrate, while the resistance comes from the surface tension. Therefore, the threshold of the tumbling motion can be considered as an outcome of two competing timescales: the visco-capillary timescale and the capillary-drag timescale, which can be, respectively, written as $\mu_1 H/\sigma_{12}$ and $\sigma_{12}/\rho_1\dot{\gamma}^3 H^3$. The ratio of the visco-capillary timescale and the capillary-drag timescale turns out to be the square of the tumbling number Tu defined in Eq. (32). Two physical implications can be obtained from this interpretation. First, when the visco-capillary timescale grows, which corresponds to increasing the dimensionless parameter Tu, the restoring process would become slower and the tumbling motion is more likely to happen. Secondly, the onset of the tumbling of the droplet portion of fluid 1 identifies the breakup of the balance between the two timescales. The threshold value of Tu could be dependent on the density ratios and viscosity ratios of the ternary fluid system. For the present cases in which the density ratios and viscosity ratios are not very large, this threshold is expected to be on the order of $O(1)$. We define the threshold value as the critical tumbling number Tu_c and depict it as a function of the Reynolds number in Fig. 15. In all case series, the critical tumbling number stably lies between 0.3 and 0.4, which validates the above implications of comparable timescales in small density–viscosity ratio scenarios. It should be noted that the droplet motion could also be influenced by the equilibrium shape of the droplet (which is associated with the contact angles), as indicated in Refs. [2,26]. However, delicately quantifying this effect would be difficult in both mathematics and physics.

4. Tumbling process

Upon the onset of tumbling motion, two consequent scenarios may arise: the tumbling-sliding (mode B-1) and the tumbling-detachment (mode B-2). In this subsection, we focus on the kinematics and dynamics of the tumbling-sliding cases, and leave the discussion of the other scenario to the next subsection. For illustration, we present the snapshots of a tumbling-sliding case at some typical time in Fig. 16. The form drag and the viscous shear stress imposed by the ambient fluid overcome the restrictions from the wall shear force and the surface tension force, which is characterized by the criticality of droplet portion of fluid 1 leaving the substrate and starting tumbling around the droplet portion of fluid 2. At this initial stage of tumbling (see the top subfigure in Fig. 16), the flow patterns remain isolated as for the sliding cases. Each portion of the compound droplet contains one major

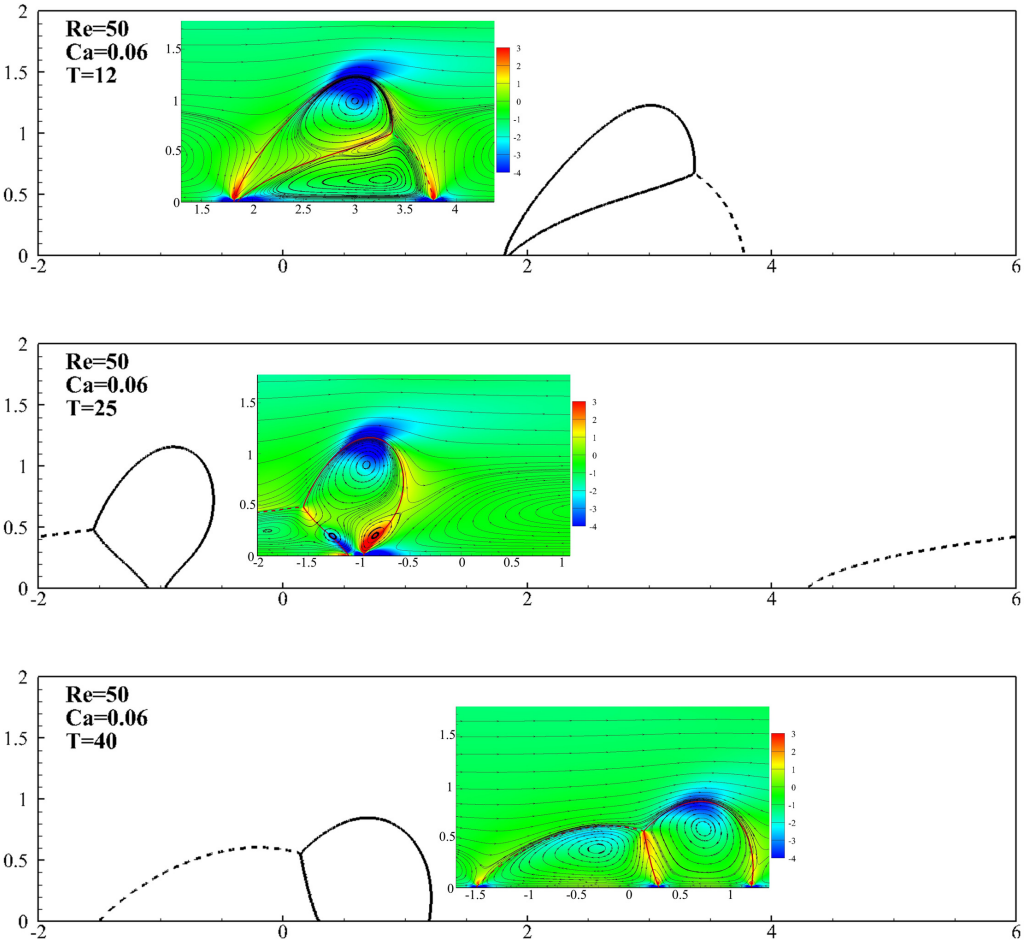

FIG. 16. Snapshots of interface locations and zoom-in views of vorticity contours and streamlines at Re=50 and Ca=0.06 in case series 1. The top subfigure snapshots the detachment of droplet portion of fluid 1 from the substrate; the middle subfigure shows the re-adhesion of the droplet portion of fluid 1 to the substrate; and the bottom subfigure illustrates the equilibrium state of quasisteady sliding. Note that the volume-averaged sliding velocity of the compound droplet has been deducted from the initial velocity field, based on which the vorticity and stream functions are calculated. Note that the left and the right boundaries of the computational domain are periodic.

vortex, while recirculation zones pertain before and after the compound droplet. The variation of the direction of surface tension force between different portions of the compound droplet contributes to the deformation of the droplet portion of fluid 2, which is shown in Fig. 17 as the stretched wetted length in this evolution stage.

A key stage of the tumbling-sliding mode discussed here is the re-adhesion of the tumbling droplet portion to the substrate, as illustrated in the middle subfigure in Fig. 16. Apart from the major vortices in each portion of the compound droplet, some minor vortices are newly generated in the vicinity of the re-adhesion point. In the meantime, the magnitude of the local vorticity is also enlarged, indicating the amplified diffusive behavior accompanied by the re-adhesion process. The re-adhesion of droplet portion of fluid 1 also imposes instant effects on the evolution of the other portion of the droplet, which is intuitively known as the removal of the surface tension force in the upstream conjunction point between these two portions. As shown in Fig. 17, the instant removal of

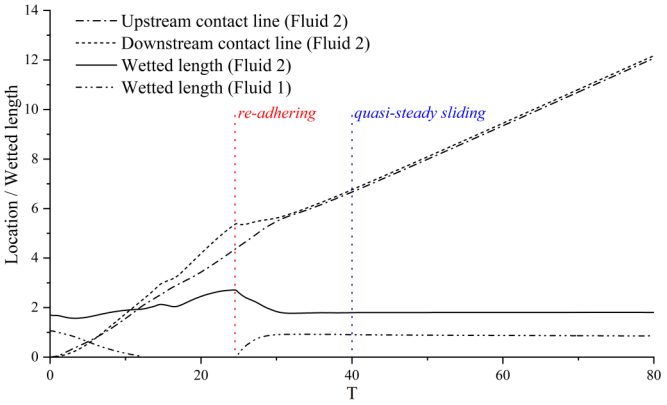

FIG. 17. Evolutions of the relative locations of the contact lines and the wetted length at Re=50 and Ca=0.06. Note that the contact-line location refers to the relative location to its initial position. Data are collected from case series 1.

this force significantly delays the propagation of the upstream contact line of the droplet portion of fluid 2 along the streamwise direction. Correspondingly, the wetted length of the droplet portion of fluid 2 continues shrinking after the re-adhesion of the droplet portion of fluid 1, until a quasisteady sliding motion is finally reached.

The quasisteady sliding motion is characterized by the steady moving velocities of the contact lines and the constant wetted length of the droplet, as shown in Fig. 17. The dynamics in such circumstances would be similar to the discussions made in Sec. III C 2.

5. Detachment dynamics

At larger capillary or Reynolds numbers, one could expect more severe deformations of the compound droplet. A typical example is the topological change of the compound droplet, which is characterized by the detachment of the droplet portion of fluid 1. The pinch-off of the droplet portion belonging to the same liquid phase, which was reported in previous work in high shear-rate scenario [31], has not been observed in the ranges of Reynolds and capillary numbers considered in this study. It should also be noted that, due to the existence of numerical diffusion, it is quite difficult to distinguish the true physical pinch-off and the numerical cutoff in simulations [40]. Therefore, we circumvent discussing the breakup of minor droplets and focus on the detachment between different fluid phases at moderate range of Reynolds numbers, although the pinch-off could exist at even higher Reynolds numbers.

Figure 18 illustrates the critical moments of two cases of detachment. The recirculation zones of the flow field roughly intersect at the detachment neck, providing necessary shear stress for the detachment. By increasing either the Reynolds or the capillary numbers, the occurrence of the detachment becomes earlier, and both portions of the compound droplet are more stretched at detachment criticality. The larger deformation can be explained by the reduced viscosity in larger Reynolds numbers and the lower restrictions of surface tension at higher capillary numbers. As shown in Fig. 19, the increased Reynolds number leads to higher vorticity values near the interfaces as well as in the near-wall region, indicating the stronger shear stress which contributes to both the spreading of the sliding droplet portion and the stretching of the tumbling droplet portion. In the meantime, the larger shear effect around the neck connecting the two portions of the compound droplet implies the quicker cutoff at higher Reynolds numbers.

Although the droplet portion of fluid 1 may detach from the compound droplet and drift in the current, the remaining droplet portion of fluid 2 remains adhered to the substrate and finally reaches a quasisliding state in all test cases considered in this work. This sliding state is due

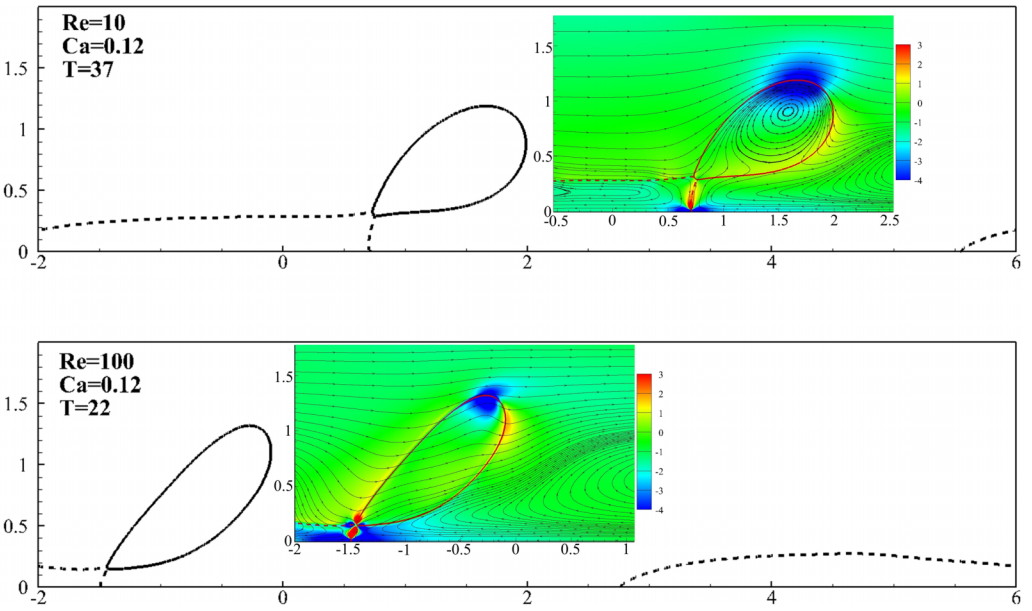

FIG. 18. Snapshots of detachment criticality for two typical cases. Zoom-in views are the local vorticity fields and streamlines near the detachment area. The volume-averaged horizontal velocity of the compound droplet has been deducted from the velocity field. The solid lines are interface of the droplet portion of fluid 1, and the dashed lines depict the interface location of the droplet portion of fluid 2. Results are from case series 1. Note that the left and the right boundaries of the computational domain are periodic.

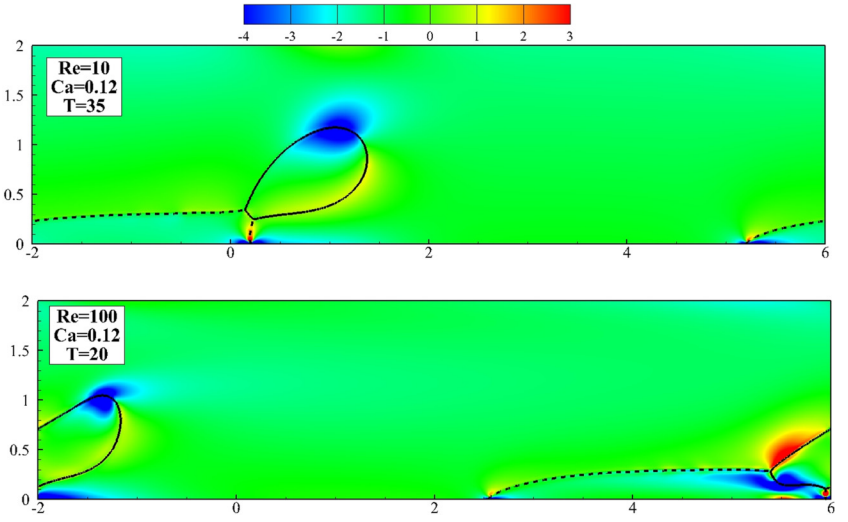

FIG. 19. Vorticity contours of the snapshots before detachment for two typical cases. The solid lines are interface of the droplet portion of fluid 1, and the dashed lines depict the interface location of the droplet portion of fluid 2. Results are from case series 1. Note that the left and the right boundaries of the computational domain are periodic.

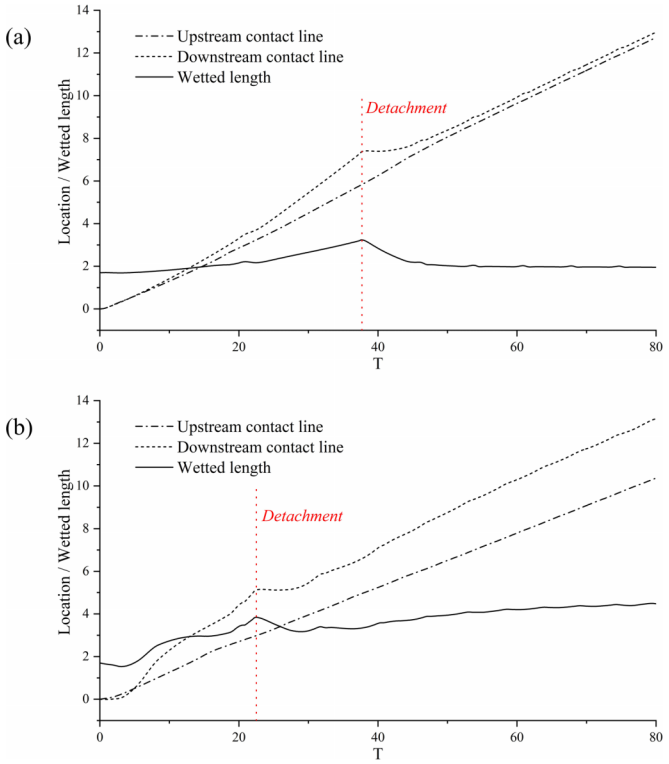

FIG. 20. Evolutions of the relative locations of the contact lines and the wetted length of the droplet portion of fluid 2 for cases of: (a) Re=10, Ca=0.12; (b) Re=100, Ca=0.12. Note that the contact-line location refers to the relative location to its initial position. Data are collected from case series 1.

to its acute contact angle with the ambient fluid, which has also been reported in the previous work of a pure droplet in shear flow [27]. To shed light on the dynamic process of detachment, the time histories of the contact-line locations and wetted length of droplet portion of fluid 2 are presented in Fig. 20. The upstream contact line, which is relatively further from the location of detachment, retains quite stable moving velocity throughout the process. Only a slight increase of propagation rate is observed upon the detachment. And, following the previous analysis of the quasisteady sliding droplet in Sec. III C 2, the converged contact-line velocities in different cases with the same capillary number would be close. This point has been demonstrated by Kang *et al.* [28] and validated in Fig. 7. The evolutions of the downstream contact line as well as the associated wetted length of the droplet portion of fluid 2, however, exhibit more complicated trends. Its initial movement could be tentatively explained as the combined effect of viscous shear stress and capillary forces. By increasing the Reynolds number, the establishment of viscous shear is delayed due to the reduced viscosity, which explains the later response of initial motion in the higher Reynolds number scenario. Upon the occurrence of detachment, the surface tension between droplet portions of fluid 1 and fluid 2 are instantly removed. Since this surface tension contributes to the stretching of the droplet portion of fluid 2 before the detachment, its vanishment leads to the retraction of the downstream contact line of this droplet portion. Accompanied with the retraction of contact line is the reduced wetted length after the detachment. An equilibrium wetted length could be achieved after sufficient time for digesting the impulse induced by detachment. Larger equilibrium wetted length can be expected at higher Reynolds number due to the reduced viscous dissipation, which has been elaborated in Sec. III C 2.

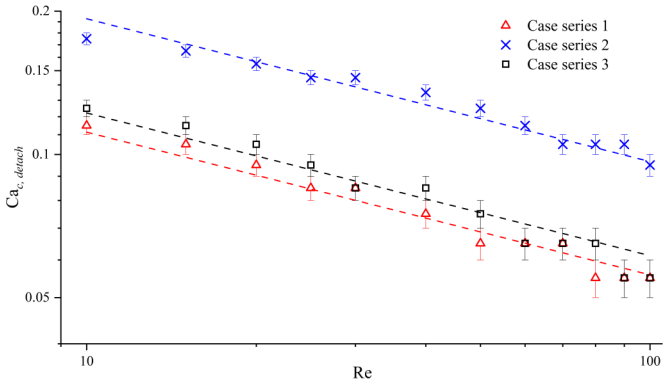

FIG. 21. Critical capillary numbers of detachment as the function of Reynolds number in log scale. The fitted lines are with the slope of $k = -0.3$.

We conclude this subsection with an overall assessment of the detachment cases recovered in the case series. Figure 21 illustrates the critical capillary number of detachments for each Reynolds number considered in our simulations. The lower limit of the error bar is the highest capillary number of the tumbling-sliding case, while the higher limit represents the smallest capillary number at which the detachment is observed. Being presented in log scale, the discrete points can be roughly fitted by a straight line with the slope of -0.3, which seemingly leads to a dimensionless number of $\mathrm{Ca}/\mathrm{Re}^{-0.3}$. Establishing a thorough physical interpretation of this relationship would be very difficult due to the many factors involved. By comparing with the tumbling number $\mathrm{Tu} = \mathrm{Ca}/\mathrm{Re}^{-0.5}$ proposed in Sec. III C 3, this fitted slope can be regarded as a transition from the tumbling number to the capillary number. It implies that the viscous shear stress and surface tension force play a more dominant role in the detachment process, whereas the importance of form drag to this process is not as significant as for the onset of tumbling.

IV. CONCLUDING REMARKS

In this work, the TPF-SMLBM is developed for simulating flows with three phases. The SMLBM is used as the flow solver that copes with the density contrast, and the ternary phase-field model is resolved by the SMLBM to evolve the interfaces. Compared with the conventional LBM for resolving this category of problems, the TPF-SMLBM directly evolves the macroscopic variables instead of the distribution functions. The number of variables at each mesh point is thus largely reduced, and both the physical boundary condition and the wetting condition on solid substrate can be directly implemented without transformation into equivalent conditions for distribution functions. Through numerical tests in two benchmark examples, the robustness of the TPF-SMLBM is established.

The compound droplet on substrate in shear is then numerically investigated using the TPF-SMLBM. The explorations were confined within the laminar regime by only studying moderate Reynolds numbers, and ignored the contact-angle hysteresis by assuming constant contact angles. Discussions of pinch-off have been circumvented to avoid possible confusions in distinguishing numerical cutoff and true physical pinch-off. Analyzing strategies utilized in previous work regarding a pure droplet have been partially referred in the present work of a compound droplet.

The kinematics of the present configuration can be categorized into three major modes: the quasisliding mode, the tumbling-sliding mode, and the tumbling-detachment mode. Flow patterns are comprehensively studied. Major vortices present in droplet portion of each fluid phase and in adjacent locations before and after the compound droplet. In the tumbling-sliding cases, upon the re-adhesion of the tumbling droplet portion to the substrate, minor vortices are generated in the interfacial region, importing extra diffusive behaviors into the flow system. In the

tumbling-detachment mode, the vicinity of the detachment point observes strong vorticity field in cases with higher Reynolds numbers, indicating that the viscous shear plays important roles in the detachment dynamics.

Dynamics of the quasisliding mode has been established through analyzing the energy absorbed by the droplet, which explains the exponential shrinking rate of the wetted length in early evolution stage. The force balance perspective paves the way of understanding the transition from the quasisliding mode to the tumbling motion, based on which a dimensionless parameter named tumbling number is defined as $\mathrm{Tu} = \mathrm{Ca}/\mathrm{Re}^{-0.5}$, where Ca and Re are the capillary number and the Reynolds number, respectively. This parameter quantifies the ratio of the promoting and the obstructing timescales of the tumbling motion, and expects a criticality on the order of $O(1)$ for the low density–viscosity ratio scenarios considered here. In addition, through abundant tests, it is found that the criticality of detachment can be scaled as $\mathrm{Ca}_{c,\mathrm{detach}} \sim \mathrm{Re}^{-0.3}$, where $\mathrm{Ca}_{c,\mathrm{detach}}$ is the critical capillary number in the occurrence of detachment. This scaling law lies between the tumbling number and the capillary number, which implies that the viscous and surface tension forces play more dominant roles in the detachment process as compared with the onset of tumbling motions.

In future studies, we expect more thorough analyses based on three-dimensional simulations and other combinations of contact angles. The difference that the contact-angle hysteresis can make in this configuration is another interesting direction. Considering scenarios with larger density or viscosity ratios and other equilibrium shapes of the compound droplet can also enrich understanding of this problem.

APPENDIX A: CHAPMAN-ENSKOG EXPANSION ANALYSIS OF LATTICE BOLTZMANN EQUATION FOR TERNARY INTERFACE TRACKING

To shed light on the equivalent macroscopic equations recovered from the lattice Boltzmann equation (15), the following expansion forms are firstly introduced:

$$\begin{aligned} h_\alpha^i &= h_\alpha^{i,(0)} + \varepsilon h_\alpha^{i,(1)} + \varepsilon^2 h_\alpha^{i,(2)} \\ \partial_t &= \varepsilon \partial_{t_0} + \varepsilon^2 \partial_{t_1} \\ \nabla &= \varepsilon \nabla_0, \end{aligned} \tag{A1}$$

where ε is a parameter proportional to the Knudsen number. Substituting the above expansions into Eq. (15), one could reveal the following formulations at different scales:

$$\varepsilon^0 : \quad h_\alpha^{i,(0)} = h_\alpha^{i,eq}, \tag{A2}$$

$$\varepsilon^1 : \quad \frac{\partial}{\partial t_0} h_\alpha^{i,(0)} + \mathbf{e}_\alpha \cdot \nabla_0 h_\alpha^{i,(0)} = -\frac{1}{\tau_i \delta_t} h_\alpha^{i,(1)}, \tag{A3}$$

$$\varepsilon^2 : \quad \frac{\partial}{\partial t_1} h_\alpha^{i,(0)} + \frac{\partial}{\partial t_0}\left(1 - \frac{1}{2\tau_i}\right) h_\alpha^{i,(1)} + \mathbf{e}_\alpha \cdot \nabla_0 \left(1 - \frac{1}{2\tau_i}\right) h_\alpha^{i,(1)} = -\frac{1}{\tau_i \delta_t} h_\alpha^{i,(2)}. \tag{A4}$$

Equations (A2) and (A3) establish the connection between the nonequilibrium and the equilibrium parts of the distribution function as

$$\varepsilon h_\alpha^{i,(1)} = -\tau_i \delta_t \left(\frac{\partial}{\partial t} + \mathbf{e}_\alpha \cdot \nabla\right) h_\alpha^{i,eq} = -\tau_i \delta_t D h_\alpha^{i,eq}, \tag{A5}$$

where $D = \partial_t + \mathbf{e}_\alpha \cdot \nabla$ is a derivative operator. Equation (A2) also indicates that the nonequilibrium parts take no net effect on the macroscopic variables when being summed up, meaning that

$$\sum_\alpha h_\alpha^{i,(0)} = \sum_\alpha h_\alpha^{i,eq} = \sum_\alpha h_\alpha^i = \varphi_i, \tag{A6}$$

$$\sum_\alpha h_\alpha^{i,(1)} = \sum_\alpha h_\alpha^{i,(2)} = 0. \tag{A7}$$

With these relationships, summations of the zeroth orders of Eqs. (A3) and (A4) over all lattice velocity directions, respectively, give

$$\frac{\partial}{\partial t_0}\sum_\alpha h_\alpha^{i,(0)} + \nabla_0 \cdot \sum_\alpha \mathbf{e}_\alpha h_\alpha^{i,(0)} = 0, \tag{A8}$$

$$\frac{\partial}{\partial t_1}\sum_\alpha h_\alpha^{i,(0)} + \nabla_0 \cdot \left(1 - \frac{1}{2\tau_i}\right)\sum_\alpha \mathbf{e}_\alpha h_\alpha^{i,(1)} = 0. \tag{A9}$$

Consolidating the above two equations into the macroscopic scale leads to

$$\frac{\partial}{\partial t}\sum_\alpha h_\alpha^{i} + \nabla \cdot \sum_\alpha \mathbf{e}_\alpha h_\alpha^{i,eq} - \nabla \cdot \left(\tau_i - \frac{1}{2}\right)\delta_t \sum_\alpha \mathbf{e}_\alpha D h_\alpha^{i,eq} = 0. \tag{A10}$$

From the conservation relations, the first and the second terms in Eq. (A10) reveal the time derivative term and the convection term in Eq. (15), respectively. Using the moment relations of the equilibrium distribution function (17), the third term in Eq. (A10) can be reduced into $\nabla \cdot (\tau_i - 0.5)\eta\delta_t \nabla \mu_i$, and thus is equivalent to the diffusion term in Eq. (15) if the following relation between the relaxation parameter and the mobility holds:

$$\frac{M_0}{\lambda_i} = (\tau_i - 0.5)\eta\delta_t. \tag{A11}$$

APPENDIX B: DERIVATION OF SLBM EVOLUTION OF ORDER PARAMETERS

Recall the macroscopic Eq. (A10) recovered from the lattice Boltzmann equation of the order parameter:

$$\frac{\partial \varphi_i}{\partial t} + \nabla \cdot \sum_\alpha \mathbf{e}_\alpha h_\alpha^{i,eq} - \nabla \cdot \left(\tau_i - \frac{1}{2}\right)\delta_t \sum_\alpha \mathbf{e}_\alpha D h_\alpha^{i,eq} = 0. \tag{B1}$$

The SLBM reconstruction of the solution to the above equation consists of two steps. In the predictor step, the intermediate order parameter is proposed as

$$\varphi_i^* = \sum_\alpha h_\alpha^{eq}(\mathbf{r} - \mathbf{e}_\alpha \delta_t, t - \delta_t). \tag{B2}$$

To reveal the equivalent macroscopic equation, we implement Taylor-series expansion on the equilibrium distribution function with respect to the space and time levels of $(\mathbf{r}, t)$ and then substitute the conservation relation (A6), which yields

$$\varphi_i^* = \varphi_i(\mathbf{r}, t) - \delta_t \left[\frac{\partial \varphi_i}{\partial t} + \nabla \cdot \sum_\alpha \mathbf{e}_\alpha h_\alpha^{i,eq} - \frac{\delta_t}{2}\nabla \cdot \sum_\alpha \mathbf{e}_\alpha D h_\alpha^{i,eq} + O\left(\delta_t^2\right)\right]. \tag{B3}$$

The formula within the square bracket of Eq. (B3) represents a second-order accurate equation recovered from Eq. (B2). To finally reach the desired phase-field equation (B1), the following macroscopic equation is tailored in the corrector step:

$$\frac{\partial \varphi_i}{\partial t} - \nabla \cdot (\tau_i - 1)\delta_t \sum_\alpha \mathbf{e}_\alpha D h_\alpha^{i,eq} = 0. \tag{B4}$$

Using the central difference scheme to discretize the above equation, one can construct the following evolution equation for the corrector step:

$$\varphi_i(\mathbf{r},\ t) = \varphi_i^* + \sum_\alpha (\tau_i - 1)\left[\delta_t D h_\alpha^{i,eq}\left(\mathbf{r} + \frac{1}{2}\mathbf{e}_\alpha \delta_t,\ t - \frac{1}{2}\delta_t\right) - \delta_t D h_\alpha^{i,eq}\left(\mathbf{r} - \frac{1}{2}\mathbf{e}_\alpha \delta_t,\ t - \frac{1}{2}\delta_t\right)\right]. \tag{B5}$$

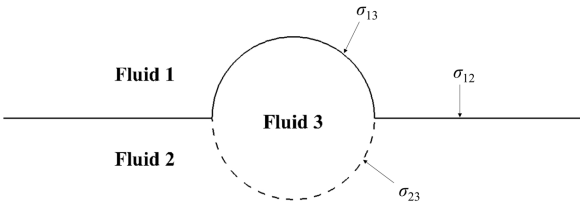

FIG. 22. Schematic diagram of the spreading liquid lens. The solid lines and the dashed lines represent the interfaces of fluid 1 and fluid 2, respectively.

Equations (B2) and (B5) are essentially the evolution formulas (18) and (19) presented in Sec. II B 2.

APPENDIX C: VALIDATIONS

1. Validation case 1: Spreading of liquid lens

The spreading of a liquid lens examines the contact angles among three phases, which is a common benchmark test for ternary fluid model. The initial setup of the problem, as shown in Fig. 22, is a fluid lens placed on the interface between two layers of other fluids. The Young relation establishes the following equilibrium state at the junction point of three phases:

$$\frac{\sin\vartheta_1}{\sigma_{23}} = \frac{\sin\vartheta_2}{\sigma_{13}} = \frac{\sin\vartheta_3}{\sigma_{12}}, \tag{C1}$$

where ϑ_i is the angle occupied by phase i at the junction point (also named as the interfacial angle). The analytical formula for the distance between two triple junctions is given by

$$d = \left(\frac{2(\pi-\vartheta_1)-\sin\left(2(\pi-\vartheta_1)\right)}{8A\sin^2(\pi-\vartheta_1)} + \frac{2(\pi-\vartheta_3)-\sin\left(2(\pi-\vartheta_3)\right)}{8A\sin^2(\pi-\vartheta_3)}\right)^{-1/2}, \tag{C2}$$

where A is the area of the liquid lens.

Following the setups in Ref. [47], physical viscosities of all fluids are assumed to be equal; two cases with surface tension ratios of $(\sigma_{12}:\sigma_{13}:\sigma_{23}) = (1:1:1)$ and $(\sigma_{12}:\sigma_{13}:\sigma_{23}) = (1:0.8:1.4)$ are considered in the validation tests. Since the results should be irrelevant to the density ratios, we set high-density contrast of $(\rho_1:\rho_2:\rho_3) = (1:1.4:0.0014)$ to shed light on the stability of the solver. Note that the ratio of the largest density to the smallest one is 1000. The computational domain is discretized by uniform mesh size of 301×301. The initial diameter of the lens spans over 64 mesh spacing, and the interface thickness is set as 4 mesh spacing. The mobility parameter used in simulation is $M_0 = 0.005$. The converged results presented in Fig. 23 maintain

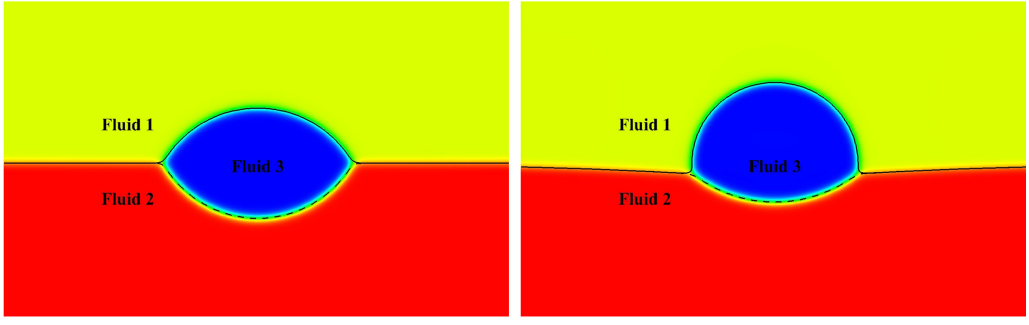

FIG. 23. Density contours and interface locations for the spreading of a liquid lens. The solid lines and the dashed lines represent the interfaces of fluid 1 and fluid 2, respectively.

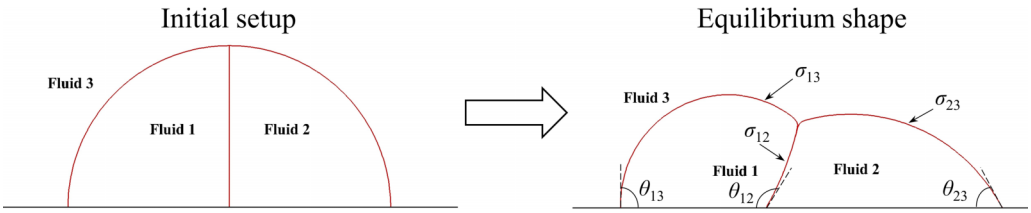

FIG. 24. Schematic diagrams of the simulation of a compound droplet on substrate.

smoothness, indicating the good stability of the solver. The computed distances between two triple junctions read 87.2 and 71.2 for the two cases, which are in good agreement with the analytical results 88.6 and 72.4, respectively.

2. Validation case 2: Compound droplet on substrate

In the second validation example, the compound droplet deposited on the solid substrate with distinct surface properties is simulated to evaluate the implementation of wetting condition in the present method. The initial setup of the problem is shown in Fig. 24. The compound droplet with equal volumes of two fluids is put on a substrate and the ambient fluid belongs to the third phase. The equilibrium shapes will be determined by the contact angles θ_{ij} which denote the angle occupied by phase i in its contact with phase j on the substrate, and the surface tensions σ_{ij} which will determine the interfacial angles at the three-phase junction point from the Young relation in Eq. (C1). The variations of density and viscosity ratios will not affect the equilibrium shapes. In the present validations, we choose $(\rho_1 : \rho_2 : \rho_3) = (1 : 0.8 : 0.1)$ and $(\nu_1 : \nu_2 : \nu_3) = (1 : 1 : 1)$. Following the previous setups [31], we consider equal surface tensions and six cases with the contact angles listed in Table II. The initial diameter of the compound droplet spans over 100 mesh spacing, the interface thickness is 3 mesh spacing, and the whole computational domain is discretized by 301×301 mesh points. The wetting condition in Eq. (13) is implemented on the top and bottom walls, while the left and right boundaries are periodic. The mobility in the simulations is $M_0 = 0.002$.

Figure 25 presents the converged results in all simulation cases, and detailed qualitative comparisons of the contact angles are shown in Table II. Note that the numerical contact angles are computed by $\theta_{ij} = (\mathbf{r}_{12} \cdot \mathbf{r}_{13})/(|\mathbf{r}_{12}| \cdot |\mathbf{r}_{13}|)$, where $\mathbf{r}_{mn} = \mathbf{r}_m - \mathbf{r}_n$. $\mathbf{r}_1$ and $\mathbf{r}_2$ are the intersecting points of the phase interface $\varphi_i = 0.5$ with the first and the second layers of mesh lines from the bottom wall; $\mathbf{r}_3$ is an arbitrary location on the bottom wall within phase i. The phase interfaces are sharp and smooth, suggesting that the method is numerically stable. The computed equilibrium contact angles are in good agreement with the analytical values, with the maximum difference within 1°, which demonstrates the accuracy of the present method in modeling ternary system with wetting

TABLE II. Comparisons of the contact angles of the compound droplet on substrate.

	θ_{12}			θ_{13}			θ_{23}		
Case no.	Analytical (°)	Ref. [31] (°)	Present (°)	Analytical (°)	Ref. [31] (°)	Present (°)	Analytical (°)	Ref. [31] (°)	Present (°)
(1)	120	120.6	119.6	90	89.1	90.1	60	59.7	59.5
(2)	90	90.0	90.1	60	59.1	60.3	60	59.1	60.8
(3)	120	120.5	120.9	120	118.4	121.0	90	89.1	89.4
(4)	60	60.7	60.3	60	60.0	60.7	90	89.1	89.4
(5)	90	90.0	89.5	90	89.1	90.2	90	89.1	90.5
(6)	60	59.7	60.8	90	89.0	89.3	120	119.4	119.2

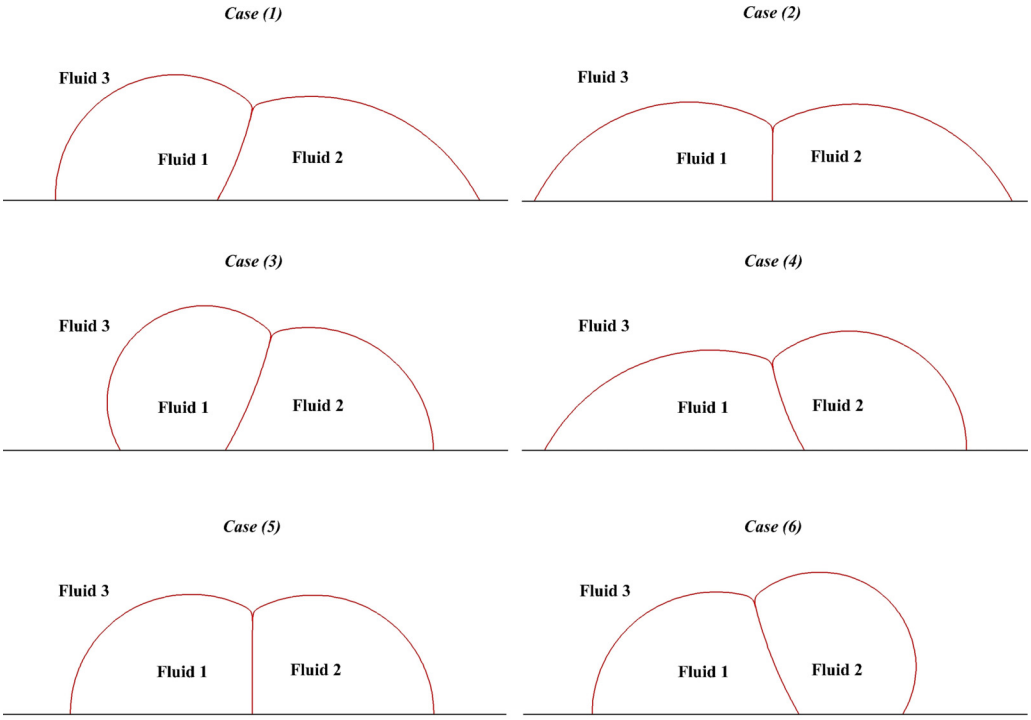

FIG. 25. Computed equilibrium shapes of compound droplet deposited on substrate.

conditions. Comparisons with previous numerical results obtained by the conventional phase-field based LBM [31] are also included in Table II, which indicates that the present method is comparably accurate as the conventional model.

[1] R. Chambers and M. Kopac, The coalescence of living cells with oil drops. I. Arbacia eggs immerised in sea water, J. Cell. Comp. Physiol. **9**, 331 (1937).

[2] P. Dimitrakopoulos and J. Higdon, On the displacement of three-dimensional fluid droplets from solid surfaces in low-Reynolds-number shear flows, J. Fluid Mech. **377**, 189 (1998).

[3] R. K. Shah, H. C. Shum, A. C. Rowat, D. Lee, J. J. Agresti, A. S. Utada, L.-Y. Chu, J.-W. Kim, A. Fernandez-Nieves, and C. J. Martinez, Designer emulsions using microfluidics, Mater. Today **11**(4), 18 (2008).

[4] K. Smith, J. Ottino, M. O. De, and La Cruz, Encapsulated Drop Breakup In Shear Flow, Phys. Rev. Lett. **93**, 204501, (2004).

[5] S.-H. Kim, H. C. Shum, J. W. Kim, J.-C. Cho, and D. A. Weitz, Multiple polymersomes for programmed release of multiple components, J. Am. Chem. Soc. **133**, 15165 (2011).

[6] D. Foresti, M. Nabavi, M. Klingauf, A. Ferrari, and D. Poulikakos, Acoustophoretic contactless transport and handling of matter in air, Proc. Natl. Acad. Sci. **110**, 12549 (2013).

[7] D. B. Kolesky, R. L. Truby, A. S. Gladman, T. A. Busbee, K. A. Homan, and J. A. Lewis, 3D bioprinting of vascularized, heterogeneous cell-laden tissue constructs, Adv. Mater. **26**, 3124 (2014).

[8] M. Nooranidoost, D. Izbassarov, S. Tasoglu, and M. Muradoglu, A computational study of droplet-based bioprinting: Effects of viscoelasticity, Phys. Fluids **31**, 081901, (2019).

[9] R. E. Johnson and S. Sadhal, Fluid mechanics of compound multiphase drops and bubbles, Annu. Rev. Fluid Mech. **17**, 289 (1985).

[10] S. Torza and S. Mason, Three-phase interactions in shear and electrical fields, J. Colloid Interface Sci. **33**, 67 (1970).
[11] S. Sadhal and R. E. Johnson, Stokes flow past bubbles and drops partially coated with thin films. Part 1. Stagnant cap of surfactant film–exact solution, J. Fluid Mech. **126**, 237 (1983).
[12] Y. H. Mori, Configurations of gas-liquid two-phase bubbles in immiscible liquid media, Int. J. Multiphase Flow **4**, 383 (1978).
[13] I. B. Bazhlekov, P. J. Shopov, and Z. D. Zapryanov, Unsteady motion of a type-A compound multiphase drop at moderate Reynolds numbers, J. Colloid Interface Sci. **169**, 1 (1995).
[14] J. Li, H. Chen, and H. A. Stone, Breakup of double emulsion droplets in a tapered nozzle, Langmuir **27**, 4324 (2011).
[15] Y. Chen, X. Liu, and Y. Zhao, Deformation dynamics of double emulsion droplet under shear, Appl. Phys. Lett. **106**, 141601, (2015).
[16] J. Wang, X. Wang, M. Tai, and J. Guan, Oriented shift and inverse of the daughter droplet due to the asymmetry of grand-daughter droplets of multiple emulsions in a symmetric flow field, Appl. Phys. Lett. **108**, 021603, (2016).
[17] T. V. Vu, Parametric study of the collision modes of compound droplets in simple shear flow, Int. J. Heat Fluid Flow **79**, 108470, (2019).
[18] H. Hua, J. Shin, and J. Kim, Dynamics of a compound droplet in shear flow, Int. J. Heat Fluid Flow **50**, 63 (2014).
[19] H. Liu, Y. Lu, S. Li, Y. Yu, and K. C. Sahu, Deformation and breakup of a compound droplet in three-dimensional oscillatory shear flow, Int. J. Multiphase Flow **134**, 103472 (2021).
[20] Z. Y. Luo, L. He, and B. F. Bai, Deformation of spherical compound capsules in simple shear flow, J. Fluid Mech. **775**, 77 (2015).
[21] S. K. Veerapaneni, Y.-N. Young, P. M. Vlahovska, and J. Bławzdziewicz, Dynamics of a Compound Vesicle in Shear Flow, Phys. Rev. Lett. **106**, 158103, (2011).
[22] P.-G. De Gennes, Wetting: Statics and dynamics, Rev. Mod. Phys. **57**, 827, (1985).
[23] P. Dimitrakopoulos and J. Higdon, On the displacement of three-dimensional fluid droplets adhering to a plane wall in viscous pressure-driven flows, J. Fluid Mech. **435**, 327, (2001).
[24] P. Dimitrakopoulos, Deformation of a droplet adhering to a solid surface in shear flow: Onset of interfacial sliding, J. Fluid Mech. **580**, 451 (2007).
[25] P. D. Spelt, Shear flow past two-dimensional droplets pinned or moving on an adhering channel wall at moderate Reynolds numbers: A numerical study, J. Fluid Mech. **561**, 439 (2006).
[26] H. Ding and P. D. Spelt, Onset of motion of a 3D droplet on a wall in shear flow at moderate Reynolds numbers, J. Fluid Mech. **599**, 341 (2008).
[27] H. Ding, M. N. Gilani, and P. D. Spelt, Sliding, pinch-off and detachment of a droplet on a wall in shear flow, J. Fluid Mech. **644**, 217, (2010).
[28] Q. Kang, D. Zhang, and S. Chen, Displacement of a three-dimensional immiscible droplet in a duct, J. Fluid Mech. **545**, 41 (2005).
[29] C.-Y. Zhang, H. Ding, P. Gao, and Y.-L. Wu, Diffuse interface simulation of ternary fluids in contact with solid, J. Comput. Phys. **309**, 37 (2016).
[30] H. Ding and P. D. Spelt, Wetting condition in diffuse interface simulations of contact line motion, Phys. Rev. E **75**, 046708 (2007).
[31] Y. Yu, D. Liang, and H. Liu, Lattice Boltzmann simulation of immiscible three-phase flows with contact-line dynamics, Phys. Rev. E **99**, 013308, (2019).
[32] X. Shang, Z. Luo, and B. Bai, Numerical simulation of dynamic behavior of compound droplets on solid surface in shear flow by front-tracing method, Chem. Eng. Sci. **193**, 325 (2019).
[33] S. Van der Graaf, T. Nisisako, C. Schroën, R. Van Der Sman, and R. Boom, Lattice Boltzmann simulations of droplet formation in a T-shaped microchannel, Langmuir **22**, 4144 (2006).
[34] T. Inamuro, S. Tajima, and F. Ogino, Lattice Boltzmann simulation of droplet collision dynamics, Int. J. Heat Mass Transfer **47**, 4649 (2004).
[35] A. Mazloomi Moqaddam, S. S. Chikatamarla, and I. V. Karlin, Simulation of binary droplet collisions with the entropic lattice Boltzmann method, Phys. Fluids **28**, 022106, (2016).

[36] A. Fakhari, M. Geier, and T. Lee, A mass-conserving lattice Boltzmann method with dynamic grid refinement for immiscible two-phase flows, J. Comput. Phys. **315**, 434 (2016).
[37] K. A. Raman, R. K. Jaiman, T.-S. Lee, and H.-T. Low, Lattice Boltzmann simulations of droplet impact onto surfaces with varying wettabilities, Int. J. Heat Mass Transfer **95**, 336 (2016).
[38] Z. Chen and C. Shu, *Simplified And Highly Stable Lattice Boltzmann Method: Theory And Applications* (World Scientific, Singapore, 2020).
[39] Z. Chen, C. Shu, D. Tan, X. Niu, and Q. Li, Simplified multiphase lattice Boltzmann method for simulating multiphase flows with large density ratios and complex interfaces, Phys. Rev. E **98**, 063314, (2018).
[40] C. Josserand, P. Ray, and S. Zaleski, Droplet impact on a thin liquid film: Anatomy of the splash, J. Fluid Mech. **802**, 775 (2016).
[41] X. He, S. Chen, and R. Zhang, A lattice Boltzmann scheme for incompressible multiphase flow and its application in simulation of Rayleigh–Taylor instability, J. Comput. Phys. **152**, 642 (1999).
[42] F. Boyer and C. Lapuerta, Study of a three component Cahn-Hilliard flow model, ESAIM: Mathematical Modelling and Numerical Analysis **40**, 653 (2006).
[43] J. Huang, C. Shu, and Y. Chew, Mobility-dependent bifurcations in capillarity-driven two-phase fluid systems by using a lattice Boltzmann phase-field model, Int. J. Numer. Methods Fluids **60**, 203 (2009).
[44] G. Seevaratnam, H. Ding, O. Michel, J. Heng, and O. Matar, Laminar flow deformation of a droplet adhering to a wall in a channel, Chem. Eng. Sci. **65**, 4523 (2010).
[45] J. Eggers, Universal Pinching of 3D Axisymmetric Free-Surface Flow, Phys. Rev. Lett. **71**, 3458 (1993).
[46] G. H. McKinley and M. Renardy, Wolfgang von Ohnesorge, Phys. Fluids **23**, 127101 (2011).
[47] Y. Shi, G. Tang, and Y. Wang, Simulation of three-component fluid flows using the multiphase lattice Boltzmann flux solver, J. Comput. Phys. **314**, 228 (2016).